CrossMark

J. Fluid Mech. (2015), *vol.* 770, *pp.* 52–84. © Cambridge University Press 2015
doi:10.1017/jfm.2015.135

Flow in a meandering channel

J. M. Floryan†

Department of Mechanical and Materials Engineering, The University of Western Ontario, London, Ontario, N6A 5B9, Canada

(Received 30 August 2013; revised 5 August 2014; accepted 2 March 2015; first published online 30 March 2015)

A comprehensive analysis of the pressure-gradient driven flow in a meandering channel has been presented. This geometry is of interest as it can be used for the creation of streamwise vortices which magnify the transverse transport of scalar quantities, e.g. heat transfer. The linear stability theory has been used to determine the meandering wavelengths required for the vortex formation. It has been demonstrated that reduction of the wavelength results in the onset of flow separation which, when combined with the wall geometry, results in an effective channel narrowing: the stream 'lifts up' above the wall and becomes nearly rectilinear, thus eliminating vortex-generating centrifugal forces. Increase of the wavelength also leads to a nearly rectilinear stream, as the slope of the wall modulations becomes negligible. As shear-driven instability may interfere with the formation of vortices, the conditions leading to the onset of such instability have also been investigated. The attributes of the geometry which lead to the most effective vortex generation without any interference from the shear instabilities and with the smallest drag penalty have been identified.

Key words: flow control, mixing enhancement, transition to turbulence

1. Introduction

Intensification of heat transfer in various flow passages of practical importance has always been of interest. The intensification schemes can be divided into those involving changes in the effective thermophysical properties of fluids and those involving improvement in fluid mixing (Bergles & Webb 1985; Bergles, Jensen & Shome 1996; Ligrani, Oliveira & Blaskovitch 2003). Enhanced mixing is of special interest in compact heat exchangers operating at low Reynolds numbers where the flow is laminar (Webb & Bergles 1983). It is generally believed that better mixing can be obtained either by forcing the laminar–turbulent transition under subcritical conditions or by introducing vortex generators, which are effective but come with a large pressure drag penalty (Jacobi & Shah 1995; Fiebeg 1995*a*,*b*, 1998; Fiebeg & Chen 1999). An alternative approach relies on the use of hydrodynamic instabilities that modify the laminar states without necessarily inducing the laminar–turbulent transition. A good illustration is offered by the technique based on the use of transverse grooves that force local flow separation; the flow is driven with a small oscillatory component and enters into resonance with instabilities of the separated shear layer (Patera & Mikic 1986). Centrifugal instability represents another illustration, as it is able to create

† Email address for correspondence: mfloryan@eng.uwo.ca

https://doi.org/10.1017/jfm.2015.135 Published online by Cambridge University Press

streamwise vortices without the large drag penalty associated with the standard vortex generators. Even when the flow is marginally stable, the instability may assist the vortex generators in reducing the decay rate of vortices, thus reducing the required number of such generators. Streamwise vortices can increase heat transfer directly by creating transverse convection, as well as indirectly by giving rise to a bypass transition. The latter process consists of a rapid three-dimensionalization of the flow field, formation of transverse shear layers with inflection points and a rapid growth of secondary instabilities (Floryan 1991). An alternative method that relies on the maximization of heat conduction through the use of properly shaped grooves while, at the same time, reducing the flow pressure losses, has been proposed recently (Moradi & Floryan 2013*b*). This method offers an alternative to the most common enhancement schemes used in micro-channels (Gong *et al.* 2011).

The fact that turning shear layers are subject to centrifugal instability has been known for almost 100 years. This instability has been studied in the case of simple geometries and reference canonical flows where the curvature of streamlines can be easily predicted and/or approximated. Rayleigh (1920) described the inviscid mechanism in the case of flow between rotating cylinders and expressed the necessary stability condition in terms of the distribution of circulation. Taylor (1923) considered the full viscous problem and determined the critical conditions for the onset of the secondary flow. Dean (1928) analysed similar instability in curved channels. Görtler (1941) demonstrated the existence of centrifugal instability in the case of boundary layers over concave surfaces. Floryan (1986) showed that the instability is active in flows over concave as well as convex surfaces if the streamwise velocity distribution is non-monotonic. In all these studies the wall curvature was either constant or had been approximated as a constant providing an explicit relation between the streamline curvature and the wall curvature. As a result, it was possible to describe the critical stability conditions in terms of a single parameter.

Theoretical analyses which can identify the onset conditions for flows in complex geometries, where the wall curvature varies spatially, are very limited. There is, however, a plethora of numerical simulations as well as experimental investigations that provide qualitative information. The existence of streamwise vortices attributed to the centrifugal instability in sinusoidal channels has been demonstrated experimentally by Gschwind, Regele & Kottke (1995), who used a meandering amplitude of the same order of magnitude as the channel height, and Nishimura *et al.* (1990*a*,*b*), who used a large amplitude compared to the channel height. Other forms of instability for similar geometries have been documented qualitatively by Rush, Newell & Jacobi (1999). The theoretical analyses, which used two-dimensional models, were able to assess the effects of flow separation on the heat transfer (Metwally & Manglik 2004; Zhang, Kundu & Manglik 2004) as well as identified conditions leading to self-sustained oscillations either through single or double Hopf bifurcations (Guzmán *et al.* 2009). Such models were unable to predict the onset of the vortices. Sui, Teo & Lee (2012) considered a three-dimensional channel of rectangular cross-section with very large amplitude of meandering, and used numerical simulations to identify a complex pattern of Dean's vortices that evolved both spatially and temporally. Pham, Plourde & Doan (2008) identified coherent structures in the case of turbulent flow. Centrifugal instability has been also found in other classes of geometries, i.e. boundary layer flows over wavy surfaces (Saric & Benmalik 1991), Couette flows over wavy walls (Floryan 2002), flows in converging–diverging channels (Floryan 2003) and flows in contracting–expanding tubes (Loh & Blackburn 2011). Recent results show that a proper distribution of triangular surface obstacles is capable of inducing streamwise

https://doi.org/10.1017/jfm.2015.135 Published online by Cambridge University Press

vortices (Floryan & Asai 2011). Extension of meandering patterns into the third dimension results in the formation of secondary vortex-like structures (Rosaguti, Fletcher & Haynes 2007), which can lead to a chaotic flow response (Castelain *et al.* 1997, 2001).

The structure of the centrifugal force field depends on the form of meandering. Since the number of possible forms is infinite, this analysis is focused on a well-defined reference case, i.e. sinusoidal meandering, which is described in terms of two parameters, i.e. the wavenumber and the amplitude. The reader may note that such sinusoidal meandering is likely to represent an arbitrary meandering with the same wavelength and amplitude if one invokes the reduced geometry concept (Floryan 2007). As the force field changes from stabilizing to destabilizing along the channel axis and across the channel, the stability conditions depend on whether the driving mechanism in the area where the force field is destabilizing is strong enough to maintain the secondary flow throughout the channel. The more general question, i.e. identification of the optimal form of meandering that leads to the generation of vortices either at the lowest *Re* or at the smallest cost expressed in terms of the additional pressure loss, remains to be answered. Since it is known that various forms of channel distortions may lead to drag reduction (Mohammadi & Floryan 2013*a*,*b*; Moradi & Floryan 2013*a*), it might be possible to utilize these effects for further reduction of the pressure loss. An interesting alternative for the reduction of pressure loss is offered by the use of periodic heating (Hossain, Floryan & Floryan 2012).

The flow may become unstable for various combinations of the meandering wavenumber and amplitude, with the critical Reynolds number being different in each case. The critical conditions can be determined using linear stability theory. Since the pressure losses increase as the surface corrugations become more extreme (Mohammadi & Floryan 2013*a*), the primary interest in this work is in 'shallow' meandering in order to determine the onset conditions that can be achieved with the smallest pressure loss. The reader should note that the more pronounced meandering is likely to lead to a more intense instability. However, meandering that becomes too extreme may lead to flow separation with separation bubbles 'smoothing out' the geometry, reducing the strength of the centrifugal force field and thus eliminating vortices (Nishimura *et al.* 1990*a*,*b*; Oviedo-Tolentino *et al.* 2008). The global critical Reynolds number, i.e. the largest stable *Re* for the specified amplitude of meandering regardless of its wavelength, is also sought as it defines the minimal conditions required for the creation of the vortices.

The meandering flow may be subject to the travelling wave (TS) instability. It is either this instability or the centrifugal instability that may dominate the system response. Little is known about the TS instability in meandering channels, and thus it is necessary to carry out its analysis together with the analysis of the centrifugal instability. Another complication is associated with the transient, non-modal disturbance growth (Schmid 2007) which may dominate the instability process if the flow environment is noisy. It has been shown that the optimal disturbance, i.e. the disturbance that results in the optimal growth, has the form of streamwise vortices in the case of corrugated walls (Szumbarski & Floryan 2006). Comparison of the temporal growth with the growth associated with the modal (asymptotic) instability shows that the former may amplify disturbances by a factor of 500–1000 before the modal instability catches up. A quiescent environment is assumed in the current analysis and therefore the transient growth is not considered. If the background noise had a uniform distribution, the streamwise vortices would emerge from the instability and they would assume the form determined by the asymptotic

https://doi.org/10.1017/jfm.2015.135 Published online by Cambridge University Press

theory (Szumbarski & Floryan 2006). Thus the omission of the temporal growth does not affect predictions based on the asymptotic stability. The presence of a non-uniform background noise may give preference to a particular disturbance form which would invalidate the predictions presented in this paper. Accurate predictions for a noisy environment would require access to complete information about the structure of the background noise. Bai & Yang (2011) carried out a two-dimensional asymptotic stability analysis using a small boundary curvature assumption and ended up with modified Orr–Sommerfeld; their assumptions are too restrictive to provide any guidance for the present analysis.

The present work does not address the problem of river meandering. River flow is an open flow driven by gravity, with erosion playing a significant role and leading to changes in the river direction, i.e. meandering. The relevant mechanics has been extensively studied, e.g. Parker (1976), Ikeda, Parker & Sawai (1981), Parker, Sawai & Ikeda (1982) and Parker & Andrews (1986). Flow in a channel is driven by a pressure gradient, the free surface plays no role and shape modifications are intentionally imposed rather than resulting from the overall system dynamics. Formation of longitudinal streaks observed in rivers (Colombini & Parker 1995) is also not related to the mechanisms leading to the vortex formation studied in this paper.

The main goal of the present analysis is the identification of channel meandering geometries that lead to the creation of streamwise vortices through the centrifugal force mechanism at a minimum cost measured by pressure losses and without interference from the travelling wave instability. This is the first comprehensive analysis of this type of flow that accounts for all possible instabilities to the best of the author's knowledge. The new knowledge would provide a rational basis for the design of compact heat exchangers operating in the laminar flow regime. The analysis is divided into three steps, i.e. (i) determination of the flow losses associated with the meandering, (ii) identification of the critical conditions required for the onset of the centrifugal and shear instabilities, and (iii) identification of geometric and flow parameters which lead to the dominance of the centrifugal instability. Section 2 provides description of steady flow and quantifies the pressure losses associated with the meandering. Section 3 describes the linear stability analysis, provides a detailed description of the vortex and travelling wave instabilities and their competition, and identifies those geometries that are the most suitable for generation of the vortices. Section 4 provides a short summary of the main conclusions.

2. Steady flow in a meandering channel

There are an infinite number of possible forms of meandering. This analysis is focused on the simplest case of a channel that follows a sinusoidal path with its geometry specified as (see figure 1)

$$\left.\begin{aligned} y_U(x) &= 1 + 2S\cos(\alpha x) = 1 + (S\mathrm{e}^{\mathrm{i}\alpha x} + \text{c.c.}),\\ y_L(x) &= -1 + 2S\cos(\alpha x) = -1 + (S\mathrm{e}^{\mathrm{i}\alpha x} + \text{c.c.}),\end{aligned}\right\} \tag{2.1}$$

where subscripts U and L refer to the upper and lower walls, respectively, the amplitude of meandering is $2S$, $\lambda = 2\pi/\alpha$ is the wavelength of one cycle of meandering, c.c. stands for the complex conjugate, and half of the mean channel opening h is used as the length scale. The channel extends from $+\infty$ to $-\infty$ in the x direction and the flow is driven by a pressure gradient.

https://doi.org/10.1017/jfm.2015.135 Published online by Cambridge University Press

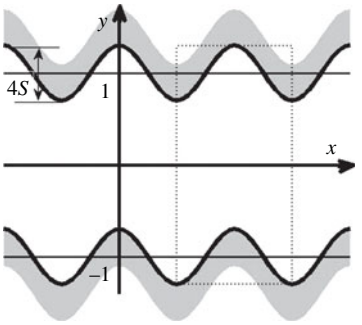


FIGURE 1. Sketch of the flow domain. The dotted line identifies the computational domain for the IBC method.

2.1. *Model problem*

The flow in a straight channel is described by the velocity $\boldsymbol{V}_0$, the pressure p_0, the stream function Ψ_0 and the flow rate Q_0 of the form

$$\left.\begin{gathered}\boldsymbol{V}_0(\boldsymbol{X}) = \left[u_0(x,y),\, v_0(x,y)\right] = \left[u_0(y),\, 0\right] = \left[1-y^2,\, 0\right], \\ p_0(\boldsymbol{X}) = -2x/Re, \\ \Psi_0(\boldsymbol{X}) = -y^3/3 + y + 2/3, \quad Q_0 = 4/3,\end{gathered}\right\} \tag{2.2}$$

where the movement of the fluid is directed towards the positive x-axis, the Reynolds number Re is defined on the basis of the maximum x-velocity and the channel half-height and $\boldsymbol{X} = (x\boldsymbol{i} + y\boldsymbol{j})$, $\boldsymbol{V}_0 = (u_0\boldsymbol{i} + v_0\boldsymbol{j})$. The flow in the meandering channel is represented as

$$\left.\begin{gathered}\boldsymbol{V}_b(\boldsymbol{X}) = \boldsymbol{V}_0(\boldsymbol{X}) + \boldsymbol{V}_1(\boldsymbol{X}) = \left[u_0(y),\, 0\right] + \left[u_1(x,y),\, v_1(x,y)\right], \\ p_b(\boldsymbol{X}) = p_0(\boldsymbol{X}) + p_1(\boldsymbol{X}), \quad \Psi_b(\boldsymbol{X}) = \Psi_0(y) + \Psi_1(x,y), \quad Q_b = Q_0 + Q_1,\end{gathered}\right\} \tag{2.3}$$

where $\boldsymbol{V}_b = (u_b\boldsymbol{i} + v_b\boldsymbol{j})$, p_b, Ψ_b, Q_b are the velocity, the pressure, the stream function and the flow rate for the complete flow, respectively, and $\boldsymbol{V}_1$, p_1, Ψ_1, Q_1 are the velocity, the pressure, the stream function and the flow rate modifications induced by the channel geometry, respectively. Substitution of (2.3) into the Navier–Stokes and continuity equations and elimination of pressure permit expression of the field equations in the form

$$\begin{aligned}&u_0\partial_x\nabla^2\Psi_1 - D^2u_0\partial_x\Psi_1 - Re^{-1}\nabla^4\Psi_1 \\ &\quad = -\partial_y\left[\partial_x\left\{u_1u_1\right\} + \partial_y\left\{u_1v_1\right\}\right] + \partial_x\left[\partial_x\left\{u_1v_1\right\} + \partial_y\left\{v_1v_1\right\}\right],\end{aligned} \tag{2.4}$$

where the curly brackets denote the velocity products and $D = \mathrm{d}/\mathrm{d}y$. The boundary conditions have the form

$$u_0\left(y_U(x)\right) + u_1\left(x, y_U(x)\right) = 0, \quad v_1\left(x, y_U(x)\right) = 0, \tag{2.5a}$$

$$u_0\left(y_L(x)\right) + u_1\left(x, y_L(x)\right) = 0, \quad v_1\left(x, y_L(x)\right) = 0. \tag{2.5b}$$

The stream function normalization is set by assuming that the total stream function becomes zero at the lower wall, i.e.

$$\Psi_0\left(y_L(x)\right) + \Psi_1\left(x, y_L(x)\right) = 0. \tag{2.6}$$

https://doi.org/10.1017/jfm.2015.135 Published online by Cambridge University Press

The problem formulation is closed by imposing the fixed mass flow rate constraint, which can be cast as

$$\Psi_0\,(y_U(x)) + \Psi_1\,\big(x,\, y_U(x)\big) = 4/3. \tag{2.7}$$

This constraint states that the mass flow rates in the straight reference channel and in the meandering channel are the same, i.e. $Q_1 = 0$. The pressure gradient correction required to drive the flow through the meandering channel can be determined by starting with the stream function expressed as a Fourier expansion of the form

$$\Psi_1(x,\, y) = \sum_{n=-\infty}^{n=+\infty} \Phi^{(n)}(y)\, \mathrm{e}^{\mathrm{i}n\alpha x}, \tag{2.8}$$

where $\Phi^{(n)} = \Phi^{(-n)^*}$ are the reality conditions and stars identify the complex conjugate. Substitution of (2.8) into (2.4) and extraction of the modal equation for $\Phi^{(0)}$ lead to

$$D^4\Phi^{(0)} + 2\alpha\, Re\, \mathrm{Im}\left(\sum_{k=1}^{k=+\infty} k\, D^2(\Phi^{(k)^*}\, D\Phi^{(k)})\right) = 0, \tag{2.9}$$

where Im denotes the imaginary part. A single integration of (2.9) gives

$$D^3\Phi^{(0)} + 2\alpha\, Re\, \mathrm{Im}\left(\sum_{k=1}^{k=+\infty} k\, D(\Phi^{(k)^*}\, D\Phi^{(k)})\right) = A\, Re, \tag{2.10}$$

where $A = \partial p_1/\partial x|_{mean}$ describes the mean pressure gradient correction; this can be demonstrated by substituting (2.3) and (2.8) into the x-momentum equation, extracting from the pressure field mode corresponding to $n = 0$ and rearranging the resulting expression.

An alternative closing constraint used in this study, the fixed pressure gradient constraint, assumes that the flows in the straight and sinusoidal channels are driven by the same pressure gradient. Change in the flow rate is then used as a measure of additional flow losses associated with the meandering. The constraint (2.7) needs to be replaced with the condition $A = 0$ and the corresponding flow rate correction Q_1 can be readily evaluated (Floryan 1997).

2.2. *Solution method and flow description*

A spectrally accurate solution is sought. The main difficulty, which arises due to the need for an efficient handling of a large number of geometric configurations parametrized by (S, α), is overcome by taking advantage of the immersed boundary condition (IBC) method (Szumbarski & Floryan 1999; Floryan 2002; Husain & Floryan 2010). This method uses a regular, fixed computational domain suitable for representing the solution in terms of expansions using the global basis functions. The flow domain is 'submerged' inside the computational domain (see figure 1), which necessitates the development of special boundary relations that ensure that the flow boundary conditions are enforced. The unknown stream function in (3.3) is represented as the Fourier expansion (3.7) and the velocity components are represented as

$$u_1(x,\, y) = \sum_{n=-\infty}^{n=+\infty} u_1^{(n)}(y)\, \mathrm{e}^{\mathrm{i}n\alpha x}, \quad v_1(x,\, y) = \sum_{n=-\infty}^{n=+\infty} v_1^{(n)}(y)\, \mathrm{e}^{\mathrm{i}n\alpha x}, \tag{2.11a,b}$$

where $u_1^{(n)} = u_1^{(n)^*}$, $v_1^{(n)} = v_1^{(n)^*}$ are the reality conditions and stars identify the complex conjugate. The modal functions in (2.8) and (2.11) are discretized using the Chebyshev

https://doi.org/10.1017/jfm.2015.135 Published online by Cambridge University Press

expansions and the Galerkin projection method is used to construct algebraic equations. The boundary constraints are imposed using the tau concept. Details of the algorithm can be found in Floryan (2002) and Husain & Floryan (2010) with the computational performance improved through the use of a specialized solver (Husain & Floryan 2013). Certain limiting cases have been solved using the domain transformation (DT) method (Husain, Floryan & Szumbarski 2009; Mohammadi & Floryan 2013*a*), where the channel is mapped analytically onto a rectangular strip and the field equations are discretized using the Fourier expansions in the streamwise direction and the Chebyshev expansions in the transverse direction. The IBC method is generally much faster computationally but the DT method is more suitable for analysis of limiting cases. Testing of the accuracy of the IBC method is discussed in § 3.1.

A simpler solution can be obtained by considering the limit $\alpha \to 0$. The flow domain is regularized using transformation $\eta = y - 2S\cos(\xi)$, where $\xi = \alpha x$ is a slow scale, resulting in the following field equations of the form

$$\alpha \frac{\partial u_b}{\partial \xi} + 2S\alpha \sin(\xi)\frac{\partial u_b}{\partial \eta} + \frac{\partial v_b}{\partial \eta} = 0, \tag{2.12a}$$

$$\begin{aligned} &-\left(1 + 4S^2\alpha^2 \sin^2(\xi)\right)\frac{\partial^2 u_b}{\partial \eta^2} - \alpha^2 \frac{\partial^2 u_b}{\partial \xi^2} - 4S\alpha^2 \sin(\xi)\frac{\partial^2 u_b}{\partial \xi \partial \eta} \\ &\quad - 2S\alpha^2 \cos(\xi)\frac{\partial u_b}{\partial \eta} + 2S\alpha\, Re\, \sin(\xi)\, u_b \frac{\partial u_b}{\partial \eta} + Re\, v_b \frac{\partial u_b}{\partial \eta} \\ &\quad + \alpha\, Re\, u_b \frac{\partial u_b}{\partial \xi} + \alpha\, Re \frac{\partial p_b}{\partial \xi} + 2S\alpha\, Re \sin(\xi)\frac{\partial p_b}{\partial \eta} = 0, \end{aligned} \tag{2.12b}$$

$$\begin{aligned} &-\left(1 + 4S^2\alpha^2 \sin^2(\xi)\right)\frac{\partial^2 v_b}{\partial \eta^2} - \alpha^2 \frac{\partial^2 v_b}{\partial \xi^2} - 4S\alpha^2 \sin(\xi)\frac{\partial^2 v_b}{\partial \xi \partial \eta} - 2S\alpha^2 \cos(\xi)\frac{\partial v_b}{\partial \eta} \\ &\quad + 2S\alpha\, Re\, \sin(\xi)\, u_b \frac{\partial v_b}{\partial \eta} + Re\, v_b \frac{\partial v_b}{\partial \eta} + \alpha\, Re\, u_b \frac{\partial v_b}{\partial \xi} + Re \frac{\partial p_b}{\partial \eta} = 0, \end{aligned} \tag{2.12c}$$

$$u_b = v_b = 0 \quad \text{at } \eta = \pm 1, \qquad Q_b = \int_{-1}^{1} u_b(\xi, \eta)\mathrm{d}\eta = \frac{4}{3}. \tag{2.12d}$$

The solution is represented as power expansions in terms of α, i.e.

$$u_b = \hat{u}_0 + \alpha^2 \hat{u}_2 + O(\alpha^3), \quad v_b = \alpha\, \hat{v}_1 + O(\alpha^3), \quad p_b = \alpha^{-1}\hat{p}_{-1} + \alpha\hat{p}_1 + O(\alpha^2), \tag{2.13a–c}$$

where

$$u_0 = (1 - \eta^2), \quad \hat{u}_2 = -\tfrac{4}{3} S\cos(\xi)\, \eta\, (1 - \eta^2), \tag{2.13d,e}$$

$$v_1 = -2S \sin(\xi)\, (1 - \eta^2), \tag{2.13f}$$

$$\hat{p}_{-1} = -2\, Re^{-1}\xi + \text{const.}, \quad \hat{p}_1 = -4S\, Re^{-1}\left[2S\xi - \eta\, \sin(\xi) + S\sin(2\xi)\right], \tag{2.13g,h}$$

$$\frac{\mathrm{d}p_b}{\mathrm{d}x} = -2\, Re^{-1} - 4\alpha^2\, S\, Re^{-1}\left[2S - y\cos(\alpha x)\right] + 0(\alpha^3), \tag{2.13i}$$

$$Re\, A = Re \left.\frac{\mathrm{d}p_1}{\mathrm{d}x}\right|_{mean} = -8\alpha^2 S^2. \tag{2.13j}$$

Equation (2.13*j*) demonstrates that the pressure losses decrease proportionally to α^2 when $\alpha \to 0$. This decrease is illustrated in figure 2(*a*). A similar solution can be developed for the fixed pressure gradient case (not shown).

https://doi.org/10.1017/jfm.2015.135 Published online by Cambridge University Press

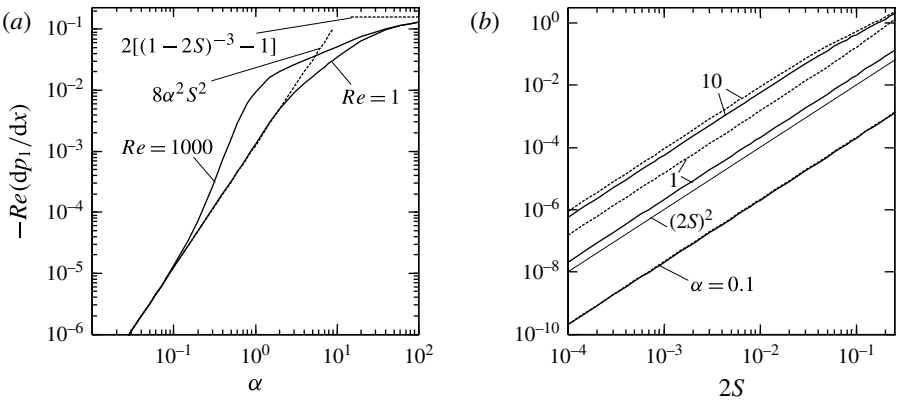


FIGURE 2. Variations of the pressure gradient correction $Re\,(\mathrm{d}p_1/\mathrm{d}x)$, (*a*) as a function of α for $S=0.0125$ and (*b*) as a function of S for $\alpha=0.1$, 1, 10. In (*b*), solid and dashed lines correspond to $Re=1$ and 1000, respectively.

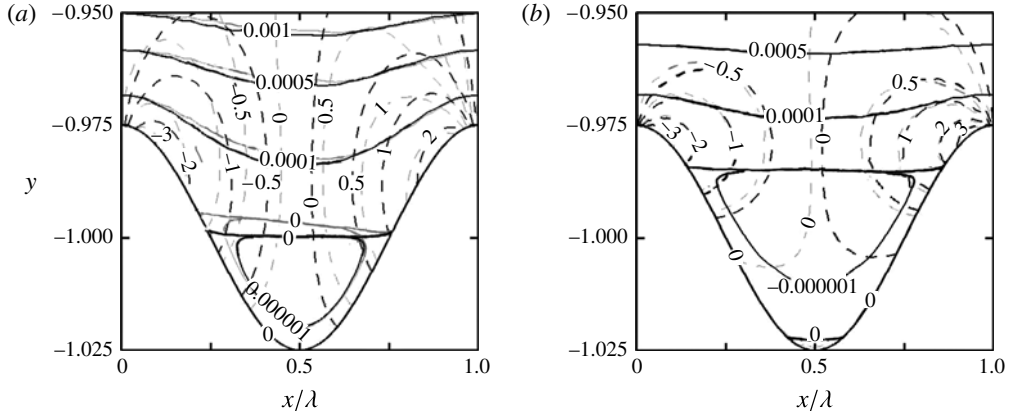


FIGURE 3. Streamlines (solid lines) and lines of constant pressure $Re\,p$ (dashed lines) in the area adjacent to the lower wall for $S=0.0125$, $Re=1$ (black lines) and $Re=1000$ (grey lines), $\alpha=50$ (*a*) and $\alpha=100$ (*b*).

Useful information about the flow properties can be deduced by considering the large wavenumber limit ($\alpha\to\infty$). Analysis of flow patterns, such as those shown in figure 3, demonstrates that a reduction of the meandering wavelength results in the formation of separation zones in the troughs. The stream lifts above the ridges and the flow becomes nearly rectilinear, eliminating the centrifugal force field. The flow assumes a form very similar to that in a smooth channel but with both walls shifted inwards by the distance $2S$ (Mohammadi & Floryan 2013*a*). It can be shown that the upper bound on the pressure gradient correction is of the form

$$Re\,A=2\left[1-(1-2S)^{-3}\right], \tag{2.14}$$

as verified by the results displayed in figure 2(*a*). The above expression provides only an upper bound as the actual flow is bounded by ridges with stagnant fluid in between, resulting in a lower shear when compared with shear at the solid wall.

https://doi.org/10.1017/jfm.2015.135 Published online by Cambridge University Press

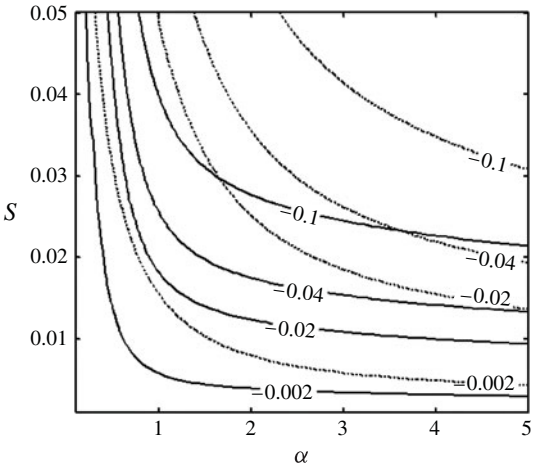


FIGURE 4. Variations of the pressure gradient correction $Re\,(\mathrm{d}p_1/\mathrm{d}x)$ as a function of S and α for $Re = 1$ (dashed lines) and $Re = 1000$ (solid lines).

The mechanics of drag formation can be explained by considering the small-amplitude meandering ($S \to 0$). Such geometries are attractive due to our interest in meandering that creates the minimum pressure loss. It is possible to show that the change in the pressure gradient is generated by the nonlinear effects and it increases proportionally with S^2 for sufficiently small S (see appendix A). Such a solution provides a good approximation even for $S = 0.1$, as demonstrated by results displayed in figure 2(*b*).

The variations of the pressure losses as a function of S and α are illustrated in figure 4. It can be seen that a reduction of the wavelength below $\alpha \approx 2$ leads to a rapid reduction of the required pressure gradient. It will be shown in the next section that such wavelengths are of most interest for the potential applications involving generation of streamwise vortices.

3. Linear stability analysis of the meandering flow

The conditions leading to the formation of streamwise vortices will be determined using the linear stability theory. The same theory can establish conditions leading to the growth of the travelling wave instability. We begin with the velocity–vorticity form of the governing equations (Floryan 1997), i.e.

$$\frac{\partial \boldsymbol{\omega}}{\partial t} - (\boldsymbol{\omega}\cdot\boldsymbol{\nabla})\boldsymbol{V} + (\boldsymbol{V}\cdot\boldsymbol{\nabla})\,\boldsymbol{\omega} = \nabla^2\boldsymbol{\omega}, \quad \boldsymbol{\nabla}\cdot\boldsymbol{V} = 0, \quad \boldsymbol{\omega} = \boldsymbol{\nabla}\times\boldsymbol{V}, \tag{3.1a–c}$$

where $\boldsymbol{\omega}$ and $\boldsymbol{V}$ are the vorticity and velocity vectors, respectively. Three-dimensional disturbances are superposed on the base flow in the form

$$\boldsymbol{\omega} = \boldsymbol{\omega}_b(x, y) + \boldsymbol{\omega}_2(x, y, z, t), \quad \boldsymbol{V} = \boldsymbol{V}_b(x, y) + \boldsymbol{V}_2(x, y, z, t), \tag{3.2a,b}$$

where the subscript b refers to the stationary flow discussed in the previous section, subscript 2 refers to the disturbance fields, and $\boldsymbol{V}_2 = (u_2, v_2, w_2)$ and $\boldsymbol{\omega}_2 = (\omega_{x2}, \omega_{y2}, \omega_{z2})$ are the disturbance velocity and vorticity vectors. The flow

https://doi.org/10.1017/jfm.2015.135 Published online by Cambridge University Press

quantities (3.2) are substituted into (3.1), the basic state is subtracted and the equations are linearized. The resulting disturbance equations have the form

$$\frac{\partial \boldsymbol{\omega}_2}{\partial t} + (\boldsymbol{V}_b \cdot \nabla)\boldsymbol{\omega}_2 - (\boldsymbol{\omega}_2 \cdot \nabla)\boldsymbol{V}_b + (\boldsymbol{V}_2 \cdot \nabla)\boldsymbol{\omega}_b - (\boldsymbol{\omega}_b \cdot \nabla)\boldsymbol{V}_2 = Re^{-1}\nabla^2\boldsymbol{\omega}_2, \tag{3.3a}$$

$$\nabla \cdot \boldsymbol{V}_2 = 0, \quad \boldsymbol{\omega}_2 = \nabla \times \boldsymbol{V}_2 \tag{3.3b,c}$$

and are subject to the homogeneous boundary conditions

$$\boldsymbol{V}_2(x, y_L, z, t) = 0, \quad \boldsymbol{V}_2(x, y_U, z, t) = 0 \tag{3.3d,e}$$

at the walls. The disturbance equation (3.3) has coefficients that are functions of x and y and thus the solution can be written in the form

$$\boldsymbol{\omega}_2(x, y, z, t) = \tilde{\boldsymbol{\omega}}_2(x, y)\, \mathrm{e}^{\mathrm{i}(\delta x + \mu z - \sigma t)} + \text{c.c.}, \tag{3.4a}$$

$$\boldsymbol{V}_2(x, y, z, t) = \tilde{\boldsymbol{V}}_2(x, y)\, \mathrm{e}^{\mathrm{i}(\delta x + \mu z - \sigma t)} + \text{c.c.}, \tag{3.4b}$$

where δ and μ are the real wavenumbers, $\tilde{\boldsymbol{\omega}}_2(x, y)$ and $\tilde{\boldsymbol{V}}_2(x, y)$ are the x-periodic amplitude functions, the real part of the exponent $\sigma = \sigma_r + \mathrm{i}\sigma_i$ describes the frequency and its imaginary part describes the growth rate, whilst c.c. stands for the complex conjugate.

The set (δ, μ, σ) represents the eigenvalues for the specified flow conditions (Re, S, α) creating a very large parameter space. To derive the eigenvalue problem for the partial differential equations (3.3) in a form that is suitable for efficient computations, we take advantage of the periodicity of the amplitude functions and represent them in terms of Fourier expansions of the form

$$\tilde{\boldsymbol{\omega}}_2(x, y) = \mathrm{i} \sum_{m=-\infty}^{m=+\infty} \left[\zeta_x^{(m)}(y), \zeta_y^{(m)}(y), \ \zeta_z^{(m)}(y)\right] \mathrm{e}^{\mathrm{i}m\alpha x}, \tag{3.5a}$$

$$\tilde{\boldsymbol{V}}_2(x, y) = \sum_{m=-\infty}^{m=+\infty} \left[g_u^{(m)}(y), \ g_v^{(m)}(y), g_w^{(m)}(y)\right] \mathrm{e}^{\mathrm{i}m\alpha x}, \tag{3.5b}$$

which leads to the following form of the disturbance quantities:

$$\boldsymbol{\omega}_2(x, y, z, t) = \mathrm{i} \sum_{m=-\infty}^{m=+\infty} \left[\zeta_x^{(m)}(y), \quad \zeta_y^{(m)}(y), \ \zeta_z^{(m)}(y)\right] \mathrm{e}^{\mathrm{i}[(\delta + m\alpha)x + \mu z - \sigma t]} + \text{c.c.}, \tag{3.6a}$$

$$\boldsymbol{V}_2(x, y, z, t) = \sum_{m=-\infty}^{m=+\infty} \left[g_u^{(m)}(y), g_v^{(m)}(y), g_w^{(m)}(y)\right] \mathrm{e}^{\mathrm{i}[(\delta + m\alpha)x + \mu z - \sigma t]} + \text{c.c.} \tag{3.6b}$$

Substitution of (3.6) into (3.3) and separation of the Fourier components, after rather lengthy algebra, results in a system of linear homogeneous ordinary differential equations of the form

$$A^{(m)}\zeta_y^{(m)} + Bg_v^{(m)} = Re \sum_{n=-\infty}^{n=+\infty} \left(H_\zeta^{(m-n)}\zeta_y^{(m-n)} + H_v^{(m-n)}g_v^{(m-n)}\right), \tag{3.7a}$$

$$C^{(m)}g_v^{(m)} = -Re \sum_{n=-\infty}^{n=+\infty} \left(I_\zeta^{(m-n)}\zeta_y^{(m-n)} + I_v^{(m-n)}g_v^{(m-n)}\right) \tag{3.7b}$$

https://doi.org/10.1017/jfm.2015.135 Published online by Cambridge University Press

for $-\infty < m < +\infty$ subject to boundary conditions (3.3*d*,*e*). In the above,

$$A^{(m)} = D^2 - k_m^2 - \mathrm{i}\,Re\,1(t_m u_0 - \sigma), \quad B = Re\,\mu D u_0, \tag{3.8a,b}$$

$$C^{(m)} = (D^2 - k_m^2)^2 - \mathrm{i}\,Re[(t_m u_0 - \sigma)(D^2 - k_m^2) - t_m D^2 u_0], \tag{3.8c}$$

$$t_m = m\alpha + \delta, \quad k_m^2 = t_m^2 + \mu^2, \tag{3.8d,e}$$

$$H_\zeta^{(m-n)} = \mathrm{i} t_m u_1^{(n)} + k_{m-n}^{-2}(\mu^2 + t_{m-n}t_m)\, v_1^{(n)} D, \tag{3.8f}$$

$$H_v^{(m-n)} = -\mu\, D u_1^{(n)} + \mathrm{i} n\alpha\mu\, k_{m-n}^{-2}\, v_1^{(n)}\, D^2, \tag{3.8g}$$

$$I_\zeta^{(m-n)} = n\alpha\,\mu\, k_{m-n}^{-2}\left[2t_{m-n}u_1^{(n)} D + (t_m + t_{m-n})\, D u_1^{(n)} - \mathrm{i}\, k_m^2 v_1^{(n)} - \mathrm{i}\, v_1^{(n)} D^2\right], \tag{3.8h}$$

$$\begin{aligned} I_v^{(m-n)} \;=\; & k_{m-n}^{-2}\left[\mathrm{i}\, n\alpha\,(\mu^2 - t_m t_{m-n})\, D u_1^{(n)} D + k_m^2(\mu^2 + t_{m-n}t_{m-2n})\, v_1^{(n)} D\right. \\ & \left. + \mathrm{i}\,(-k_{m-n}^2 t_m + 2n\alpha\mu)\; u_1^{(n)}\, D^2 + (n\alpha\, t_m - k_m^2)\, v_1^{(n)}\, D^3\right] \\ & + \mathrm{i} k_m^2 t_{m-2n} u_1^{(n)} + \mathrm{i} t_m D^2 u_1^{(n)}. \end{aligned} \tag{3.8i}$$

The above formulation uses Bloch theory (Bloch 1928) for systems with spatially periodic coefficients. It is analogous to Floquet theory (Coddington & Levinson 1965) for systems with time-periodic coefficients. The eigenvalues of the resulting system have to be determined numerically.

3.1. *Numerical solution*

Solution of the complete system requires numerical determination of the eigenvalues of (3.3*d*,*e*) and (3.7). Approximate solutions can be found by truncating the sum in (3.6) after a finite number N_M of terms and solving the eigenvalue problem for $2N_M + 1$ differential equations of type (3.7). The differential equations are discretized with spectral accuracy using Chebyshev expansions and the Galerkin projection method. The boundary conditions at the upper and lower walls are converted into the boundary relations using the IBC concept (Floryan 2002). The discretization procedure results in a matrix eigenvalue problem $\boldsymbol{\Theta}\Lambda = 0$, where $\boldsymbol{\Theta}(\sigma)$ represents the coefficient matrix. This matrix is linear in σ, i.e. $\boldsymbol{\Theta} = \boldsymbol{\Theta}_0 + \boldsymbol{\Theta}_1\sigma$, where $\boldsymbol{\Theta}_0 = \boldsymbol{\Theta}(0)$, $\boldsymbol{\Theta}_1 = \boldsymbol{\Theta}(1) - \boldsymbol{\Theta}_0$. The σ-spectrum is determined by solving a general eigenvalue problem in the form $\boldsymbol{\Theta}_0\Lambda = \sigma\boldsymbol{\Theta}_1\Lambda$. Several methods for tracing individual eigenvalues have been used, i.e. the shooting method combined with the Newton–Raphson procedure (Floryan 2002), the inverse iteration method (Floryan 2002) and Arnoldi's method (Saad 2003). The tracing of eigenvalues has been extended, if required, over several Brillouin zones (Bloch 1928) in the δ-direction in order to demonstrate how the leading eigenvalue is affected by the meandering wavelength.

The accuracy of the discretization depends on the number of Chebyshev polynomials and Fourier modes used in the solution for the mean flow, the number of Chebyshev polynomials and Fourier modes used in the solution of the disturbance equations, and the number of Fourier modes used to represent the mean flow in the numerical solution of the disturbance equations. Selection of proper numerical parameters has been done on the basis of convergence tests illustrated in tables 1 and 2 in appendix B.

https://doi.org/10.1017/jfm.2015.135 Published online by Cambridge University Press

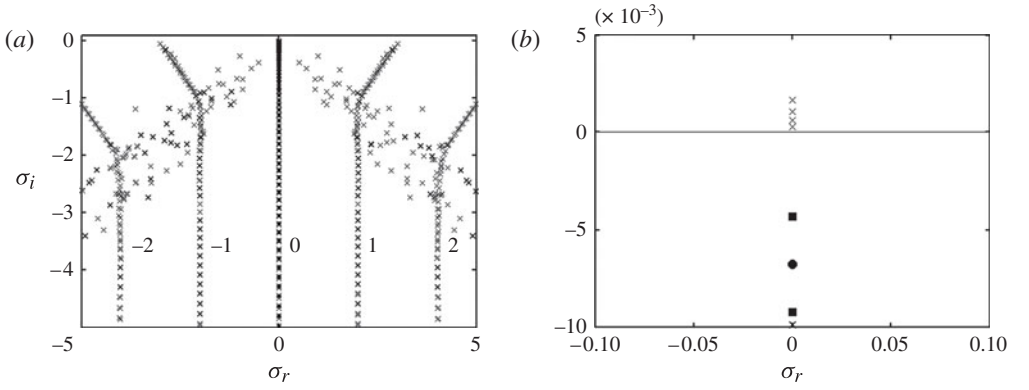


FIGURE 5. Spectrum of σ for the vortex mode for $Re = 1500$, $S = 0.02$, $\mu = 2$, $\alpha = 3$ and the fixed flow rate constraint: (*a*) complete spectrum; (*b*) enlargement focused on the main segment. Numerical symbols in (*a*) identify elements of the spectrum that correspond to different Fourier modes in (3.6) in the limit of $S \to 0$. The dots correspond to the Orr–Sommerfeld spectrum and the squares identify the Squire spectrum.

3.2. *Onset of vortices*

Channel meandering forces changes in the stream direction and this generates a centrifugal force field which, under certain conditions, may generate instability leading to the formation of streamwise vortices. Such vortices correspond to $\delta = 0$ and $\sigma_r = 0$ in (3.4). The meandering is essential for the formation of the vortices as it can be demonstrated analytically that in its absence ($S \to 0$) the vortices are attenuated (appendix C). The formation of the vortices is of practical importance as they drastically increase the heat transfer (Jacobi & Shah 1995). These vortices add transverse fluid movement, thereby taking heated fluid elements away from the hot wall and bringing cold elements into direct contact with this wall.

The centrifugal instability occurs for a sufficiently high *Re* but only if the form of the meandering satisfies certain conditions. Reduction of *Re* increases viscous dissipation and stabilizes the flow regardless of the type of meandering. The typical spectrum shown in figure 5 demonstrates the existence of many unstable modes. The vertical 'columns' of eigenvalues are associated with Fourier modes used in the numerical solution with the number of 'columns' equal to the number of Fourier modes. Four eigenvalues are unstable for *Re* used in this test. Tracing of the first two down to $S \to 0$ demonstrates that the first (most unstable) eigenvalue connects with the Tollmien–Schlichting spectrum of the smooth channel and the second eigenvalue connects with the Squire spectrum (figure 6). In the straight channel the Squire modes are less attenuated than the TS modes, but the introduction of meandering promotes amplification of the TS mode, and it is this mode, not the Squire mode, that determines the critical conditions. Evolution of the eigenfunctions $g_u^{(0)}$, $g_v^{(0)}$, $g_w^{(0)}$ for the two most unstable modes as a function of S is illustrated in figure 7.

The top eigenvalue from figure 5 has been traced in the (α, μ) space illustrating variations of the amplification rate of the most unstable mode. Results displayed in figure 8(*a*) demonstrate that meanderings that are either too 'shallow' ($\alpha \lesssim 1.5$) or too 'deep' ($\alpha \gtrsim 5.6$) do not produce instability. In the former case the flow turning is insufficient to generate a centrifugal force strong enough to create vortices, while in the latter case the stream lifts up above the ridges, which also reduces the turning

https://doi.org/10.1017/jfm.2015.135 Published online by Cambridge University Press

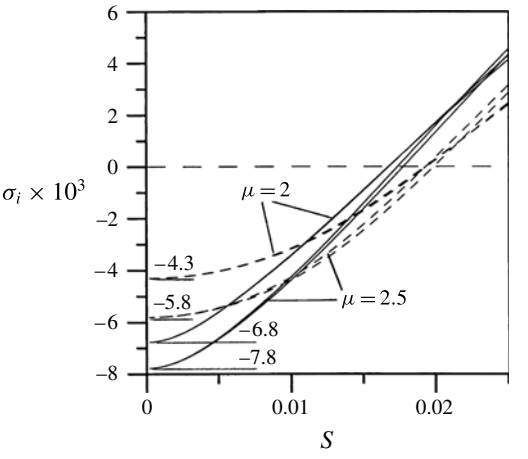


FIGURE 6. Variations of the amplification rate σ_i as a function of S for vortices with $\mu = 2$, $\mu = 2.5$ for $\alpha = 3$, $Re = 1500$ and the fixed flow rate constraint. Solid and dashed lines correspond to the first and second instability modes, respectively. See appendix C for a discussion of the limit $S \to 0$.

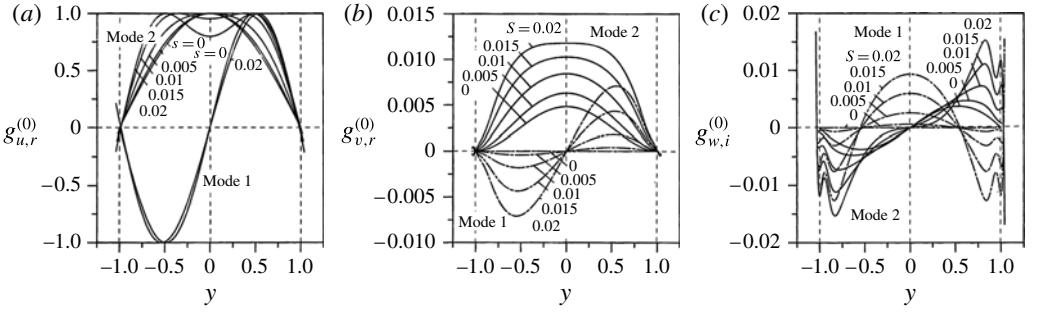


FIGURE 7. Evolution of the eigenfunctions $g^{(0)}_{u,r}$ (a), $g^{(0)}_{v,r}$ (b), $g^{(0)}_{w,i}$ (c), normalized with $\max(g^{(0)}_u) = 1$ corresponding to the first and second vortex instability modes as a function of S for $\alpha = 3$, $\mu = 2$, $Re = 1500$ and the fixed flow rate constraint.

effect and thus reduces the centrifugal force. The amplified wavelengths are contained in a finite interval of μ whose length and location are functions of α. The second mode is more stable in the sense that the range of active α is smaller, the band of the resulting vortices is narrower, and the amplification rates are smaller in comparison to the first mode (figure 8*a*).

Figures 9–11 illustrate the first three eigenfunctions for disturbance velocity components for the two most unstable instability modes. The dominant character of $\mathrm{Re}(g^{(0)}_u)$, which is the characteristic feature of the velocity field associated with the vortices (Floryan 1991), is clearly visible (see figure 9). The shape of $\mathrm{Re}(g^{(0)}_v)$ for the first mode (figure 10*a*) suggests the existence of a single layer of vortices in the middle of the channel and two layers in the case of the second mode (figure 10*b*). The same conclusion can be drawn from distributions of $\mathrm{Im}(g^{(0)}_w)$ displayed in figure 11.

The two modes give rise to very different flow topologies. These topologies are quite complex, and are illustrated in figures 12 and 13 using the velocity 'amplitude

https://doi.org/10.1017/jfm.2015.135 Published online by Cambridge University Press

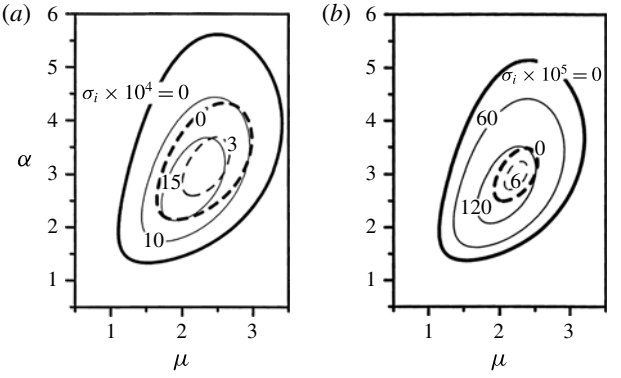


FIGURE 8. Variations of the amplification rate σ_i as a function of μ and α for vortices for $Re = 1500$, $S = 0.02$ and (*a*) the fixed flow rate constraint and (*b*) the fixed pressure gradient constraint. Solid and dashed lines correspond to the first and second instability modes, respectively.

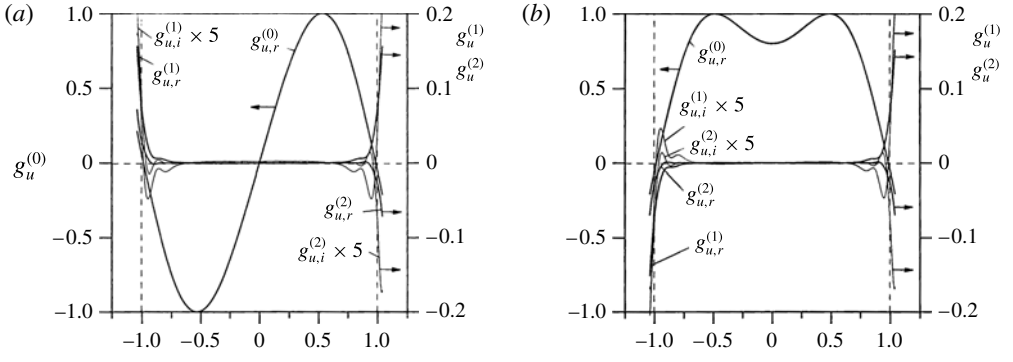


FIGURE 9. Eigenfunctions $g_u^{(m)} = g_{u,r}^{(m)} + \mathrm{i}\, g_{u,i}^{(m)}$ for the vortex mode for $m = 1, 2, 3$ normalized with condition $\max(g_u^{(0)}) = 1$ for $\mu = 2$, $\alpha = 3$, $S = 0.02$, $Re = 1500$ and the fixed flow rate constraint. (*a*) The first and (*b*) the second mode of instability.

function' $\tilde{\boldsymbol{V}}_2(x, y)$ (see (3.4)) which, in the case of vortices, can be represented as $\tilde{\boldsymbol{V}}_2(x, y) = [h_u(x, y), h_v(x, y), \mathrm{i}\, h_w(x, y)]$, where h_u, h_v, h_w are real. A change of sign of h_v provides the most reliable criterion for identification of borders between different layers of vortices. Most of the channel is 'filled in' with a single layer of vortices associated with the first mode. As the flow meanders and keeps turning up and down, additional layers form in the zones adjacent to the walls that behave as obstacles to the oncoming flow (outer walls with respect to the direction of turning; see figure 12*a*). The centrifugal effect is strongest in these locations, where it creates small vortices attached to each wall. The 'wall' vortices rotate in the same direction, alternate between the upper and lower walls and are spaced apart by half of the meandering wavelength. These vortices are the primary vortices driven directly by the centrifugal forces, while the large central vortex plays a secondary role. The centrifugal effect is not active along the wall segments that are inner with respect to the direction of turning; the primary vortices do not exist there but the secondary vortex persists due to fluid inertia. As a result, when the fluid moves in the downstream direction, the

https://doi.org/10.1017/jfm.2015.135 Published online by Cambridge University Press

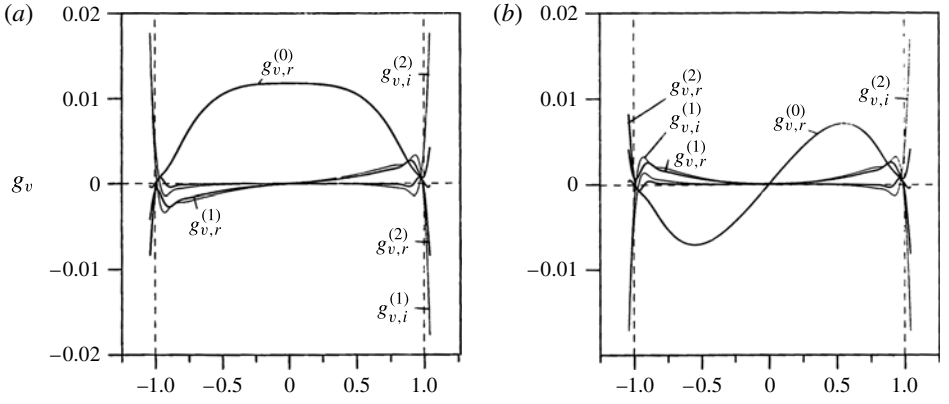


FIGURE 10. Eigenfunctions $g_v^{(m)} = g_{v,r}^{(m)} + \mathrm{i}\, g_{v,i}^{(m)}$. The remaining conditions are the same as in figure 9.

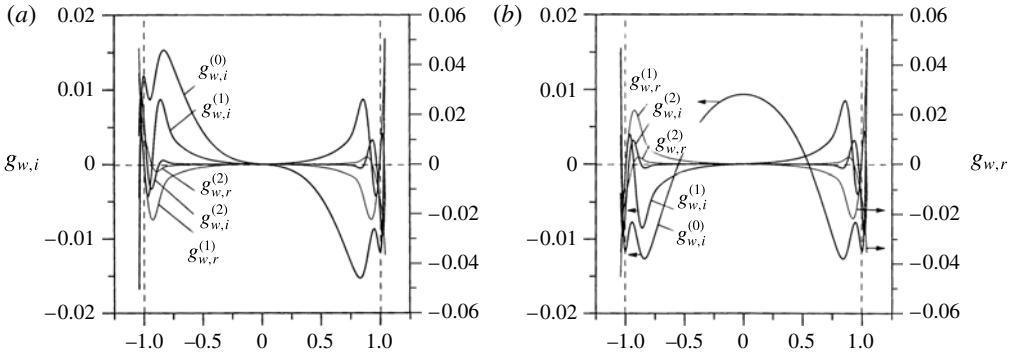


FIGURE 11. Eigenfunctions $g_w^{(m)} = g_{w,r}^{(m)} + \mathrm{i}\, g_{w,i}^{(m)}$. The remaining conditions are the same as in figure 9.

vortex motion in the central section of the channel receives a periodic boost from the primary vortices. The overall stability depends on whether this boost is strong enough to maintain the vortex motion in the area where the driving force is absent. This situation is qualitatively similar to the instability in the converging–diverging channel, where the primary vortices are located in the converging section and are able to drive the global, secondary vortices that persist through the diverging section (Floryan 2003). A similar situation is likely to occur in many other geometric configurations as long as the local primary vortices are sufficiently strong to maintain the global vortex system. Prediction of the critical conditions, however, cannot be generalized as they depend on the details of the geometry and therefore have to be analysed on a case-by-case basis.

The flow topology associated with the second mode is qualitatively similar to the first mode, as illustrated in figures 12 and 13. The primary vortices are attached to the same sections of the walls and are almost identical to those found in the case of the first mode. These ‘wall’ vortices drive two secondary vortices in the central section of the channel. The ‘wall’ vortices rotate in opposite directions in order to maintain kinematic consistency with those in the middle of the channel. Comparison

https://doi.org/10.1017/jfm.2015.135 Published online by Cambridge University Press

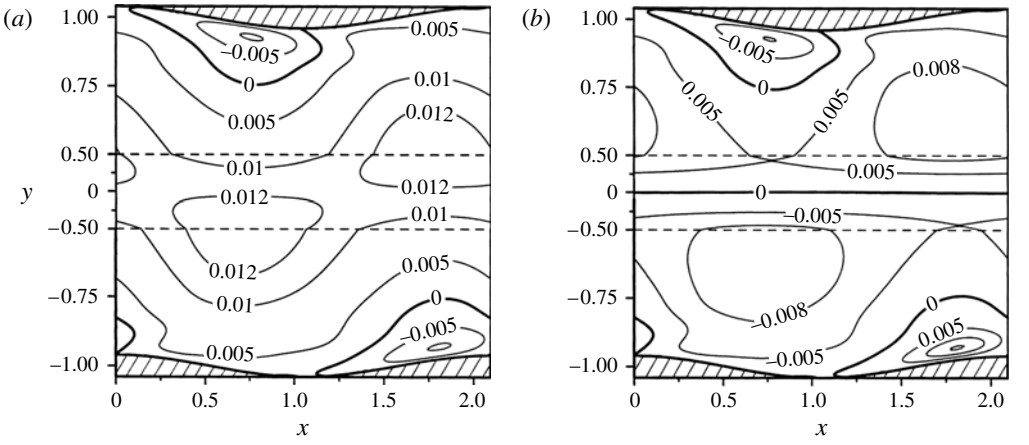


FIGURE 12. Contour plots of $h_v(x, y)$ (y-component of the velocity 'amplitude function' $\tilde{\boldsymbol{V}}_2(x, y)$; see (3.4)) for ($a$) the first and ($b$) the second instability modes. The remaining conditions are the same as in figure 9. Different layers of vortices are identified by changes of sign of h_v.

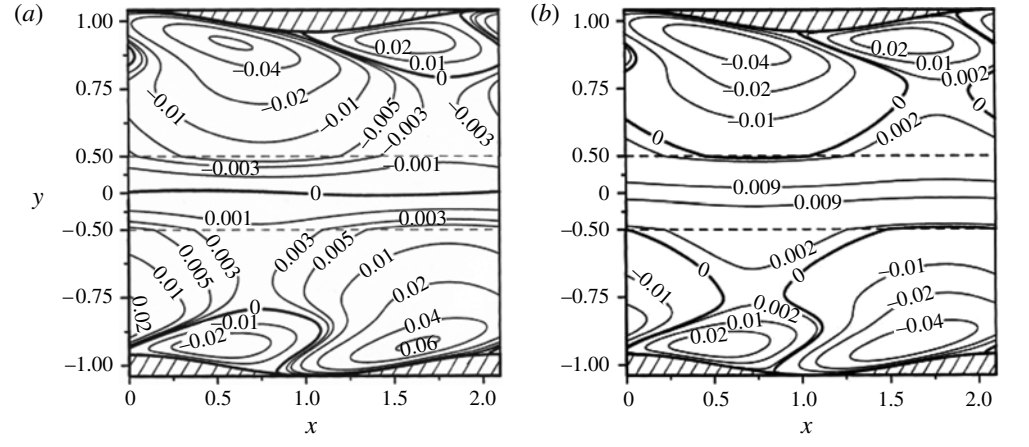


FIGURE 13. Contour plots of $h_w(x, y)$ (z-component of the velocity 'amplitude function' $\tilde{\boldsymbol{V}}_2(x, y)$; see (3.4)) for ($a$) the first and ($b$) the second instability modes. The remaining conditions are the same as in figure 9.

of figures 12(*a,b*) and 13(*a,b*) shows that the first mode is symmetric with respect to the channel axis, while the second is asymmetric. It needs to be stressed that the primary 'wall' vortices appear to be similar for both modes, with the distinction between these modes being associated with the form of the secondary, central vortices.

Figure 14(*a*) displays the neutral surfaces in the (α, μ, S) space for $Re = 1500$ for the first two modes. The first mode is always more unstable, as expected, although the second mode can be induced with a correct combination of initial conditions. There is a range of parameters where only the first mode becomes unstable. The shapes of the neutral surfaces demonstrate that the range of α leading to the instability, as well as the range of the resulting unstable μ, increase rapidly as the meandering becomes

https://doi.org/10.1017/jfm.2015.135 Published online by Cambridge University Press

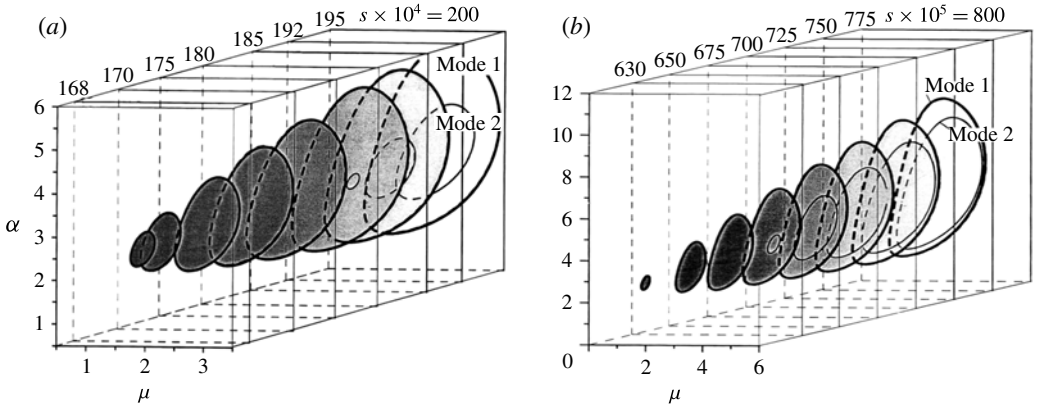


FIGURE 14. The neutral surfaces in the (α, μ, S) space for the first and second vortex instability modes for (*a*) $Re = 1500$ and (*b*) $Re = 5000$ and the fixed flow rate constraint.

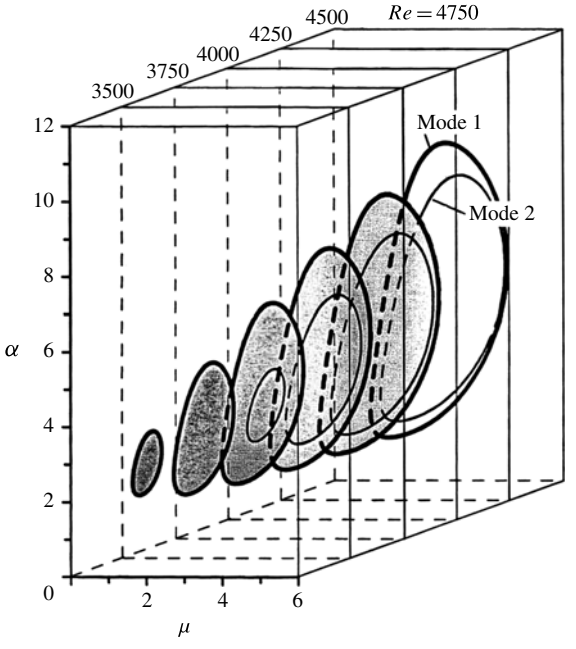


FIGURE 15. The neutral surfaces in the (α, μ, Re) space for the first and second vortex instability modes for $S = 0.008$ and the fixed flow rate constraint. The tips of the neutral surfaces define the global critical conditions $(Re_{g,cr}, \alpha_{g,cr}, \mu_{g,cr})$.

more extreme. Similar results for $Re = 5000$ displayed in figure 14(*b*) demonstrate that this increase is more rapid for higher Re, where it results in a much wider range of destabilizing α and resulting μ. It can also be seen that the instability occurs at much smaller S when Re is higher. Figure 15 displays the neutral surfaces in the (α, μ, Re) space for $S = 0.008$. A rapid increase of the range of destabilizing α and the resulting μ as Re increases is clearly visible. Meandering with wavenumbers $\alpha < 2$ is of particular interest as it provide an opportunity for the generation of vortices with smaller pressure losses.

https://doi.org/10.1017/jfm.2015.135 Published online by Cambridge University Press

The vortices play a dual role in the intensification of the heat transfer. Their appearance results in transverse fluid movement, which directly increases the heat flow. In this case the flow field consists of the reference flow with superposed vortices and the corresponding bifurcation branches are stable. The vortices may also affect the heat transfer indirectly, as they lead to a rapid three-dimensionalization of the flow field; the uplifting of the low momentum fluid away from the wall leads to the formation of highly distorted streamwise and spanwise velocity profiles which are potentially subject to very strong secondary instabilities very similar to those studied in detail in the case of Görtler instability (Floryan 1991). In this case the bifurcating branches correspond to unstable solutions and the onset of the vortices represents just the first step of the by-pass transition to turbulence. The analysis presented in this paper does not address the question of stability of the bifurcating branches. The reader may note that both types of response are possible as one may identify meandering characteristics resulting in a wide range of Re_{cr}, including those which lead to relatively small Re_{cr}. Very accurate simulations in cases where these branches are unstable document complex saturation states whose structure strongly depends on the details of the channel geometry (Guzmán *et al.* 2009; Sui *et al.* 2012). Regardless of whether one is interested in the use of vortices to promote transition or just to provide transverse advection, one would search for the least extreme meandering that leads to the onset of the instability, as this would initiate secondary effects at the lowest cost in terms of pressure loss. For presentation of the results it is convenient to introduce the global critical Reynolds number $Re_{g,cr}$, which defines the critical conditions for the onset of the instability for a given meandering amplitude S, regardless of its wavelength, as it summarizes the minimal conditions required for the creation of the vortices. Such global critical conditions correspond to the tip of the neutral surface shown in figure 15. Variations of $Re_{g,cr}$, $\alpha_{g,cr}$, $\mu_{g,cr}$ as a function of S are illustrated in figure 16 for both modes. The area below the critical curves defines the range of S and Re for which the flow is stable. The first mode determines the critical stability conditions, although the second mode can be induced with a correct selection of the initial conditions if Re is high enough. It is worth noting that $\alpha_{g,cr}$ for the second mode is about 30 % larger than for the first mode, while $\mu_{g,cr}$ is about 20 % larger.

The results presented so far have dealt with the stability of a flow that is developed under the fixed flow rate constraint. As the amplitude of meandering increases, the pressure gradient needs to be increased in order to support such a flow (§ 2). If the pressure gradient remains constant, the flow should slow down, resulting in reduction of the mass flow rate, reduction of the centrifugal effect and flow stabilization. Figure 5 displays the amplification rates for the two most unstable modes for both types of constraints. Their comparison demonstrates the relative flow stabilization associated with the fixed pressure gradient constraint. Comparison of the neutral curves for both types of flow, displayed in figure 17, underlines this stabilization and provides its quantitative measure. The onset of the instability, as measured by $Re_{g,cr}$, takes place under almost the same conditions for both types of flow, as shown in figure 16. The small difference of $Re_{g,cr}$ increases with an increase of S, with the flow with the fixed pressure gradient always being more stable. The increase of this difference is due to the progressively higher flow resistance associated with larger S (see § 2).

3.3. *Travelling wave mode*

Creation of the vortices through the centrifugal instability mechanism can be affected by the shear-driven instabilities which, once established, could prevent formation

https://doi.org/10.1017/jfm.2015.135 Published online by Cambridge University Press

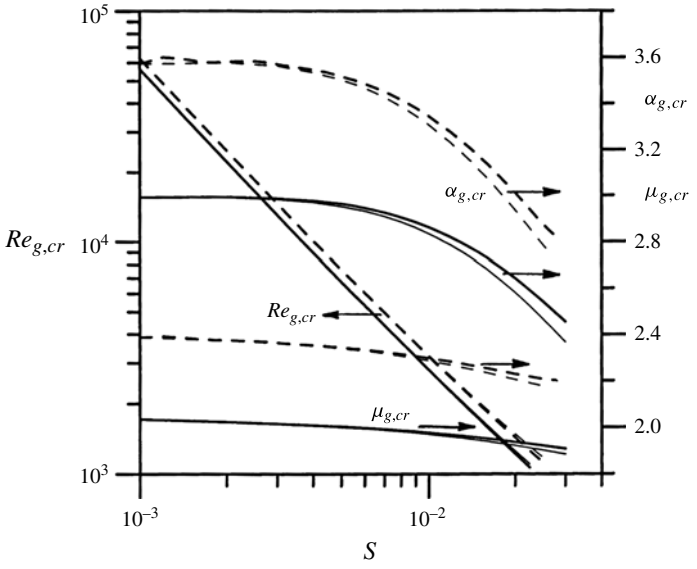


FIGURE 16. Variations of the global critical stability conditions $Re_{g,cr}$, $\alpha_{g,cr}$, $\mu_{g,cr}$ for the vortex mode as a function of S. The solid and dashed lines correspond to the first and second instability modes, respectively. The thick and thin lines correspond to the flow with the fixed flow rate and the fixed pressure gradient constraints, respectively.

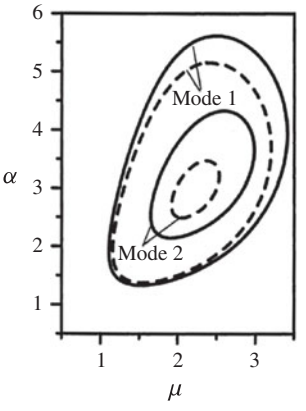


FIGURE 17. Neutral curves describing the first two modes of the vortex instability in a flow subject to the fixed flow rate constraint (solid lines) and to the fixed pressure gradient constraint (dashed lines). The remaining conditions are the same as in figure 8.

of the vortices. It is well known that flow in a straight channel is subject to the shear-driven, travelling (Tollmien–Schlichting or TS) wave instability when the Re reaches the critical value of $Re_{cr} = 5772$. The critical wave has a two-dimensional form characterized by the wavevector $(\delta_{cr}, \mu_{cr}) = (1.02, 0)$ and propagates in the downstream direction. The bifurcation has a subcritical character, and an increase in the level of background disturbances can reduce the critical Reynolds number down to $Re_{cr} \approx 2700$ (Herbert 1988).

https://doi.org/10.1017/jfm.2015.135 Published online by Cambridge University Press

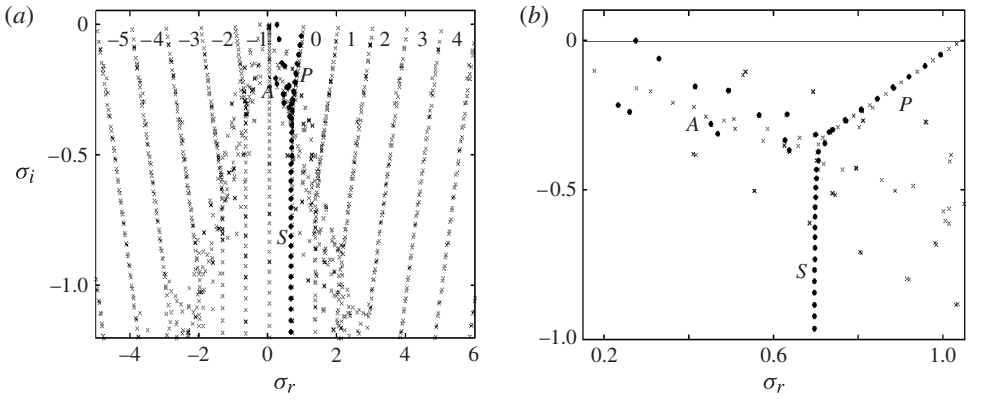


FIGURE 18. Spectrum of σ for the TS wave with the wavevector $(\delta, \mu) = (1.04, 0)$ for $S = 0.005$, $\alpha = 1$, $Re = 6000$ and the fixed flow rate constraint: (*a*) complete spectrum; (*b*) enlargement focused on the main segment. Numerical symbols in (*a*) identify elements of the spectrum that correspond to different Fourier modes in (3.6) in the limit of $S \to 0$. The A, P and S branches of the main Fourier mode (corresponding to $m = 0$ in (3.6) for $S \to 0$) are identified using the symbols A, P, S, respectively. The dots correspond to the Orr–Sommerfeld spectrum.

A typical spectrum shown in figure 18 for a two-dimensional TS wave with $(\delta, \mu) = (1.04, 0)$ for $S = 0.005$, $\alpha = 1$, $Re = 6000$ and the fixed mass constraint shows the existence of only one unstable eigenvalue. The spectrum consists of vertical 'columns', associated with different Fourier modes present in (3.5), with each segment consisting of the A, P and S branches, similar to the case of the Orr–Sommerfeld operator (Mack 1976). The Orr–Sommerfeld spectrum for the same disturbance in a straight channel is shown for comparison purposes. The complete spectrum looks like a superposition of spectra for a set of TS waves with the wavenumbers $\delta = 1.04 \pm 2$ m, with the dominant wave corresponding to $m = 0$ in (3.5), and indeed, in the limit of $S = 0$ this spectrum separates into independent segments associated with such TS waves.

Tracing of the unstable eigenvalue shown in figure 18 as a function of Re, δ, α, S provides information about the flow stability characteristics. One type of tracing, i.e. tracing of σ as a function of δ, leads to interpretation difficulties as solutions of type (3.6) are identical for $\delta = m\alpha$. The δ-axis can be divided into an infinite set of Brillouin zones with ends located at $\delta = \pm m\alpha$, with identical variations of σ_i in each zone. Values of δ that are of physical interest may extend over several Brillouin zones, and therefore one has to identify proper connections between different branches in each Brillouin zone in order to construct a continuous and physically relevant relation $\sigma_i(\delta)$ extending over the range of δ of physical interest. There are multiple relations with the property $\sigma_i(\delta) = \sigma_i(\delta + m\alpha)$, which makes some of the eigenvalues in the spectrum shown in figure 18 physically irrelevant as they belong to curve $\sigma_i(\delta)$ shifted by $n\alpha$ in the δ-direction. Several of the top eigenvalues in this spectrum correspond to branches associated with modes $\pm m$, each of which has a similar periodicity in the δ-direction, and this adds to the interpretation difficulties. Variations of the physically relevant eigenvalues as a function of δ can nevertheless be traced, with the inverse iteration being the most reliable tracing method. The reliability of the tracing was verified by studying modal shapes and by taking the limit of $S \to 0$ to make sure that the correct mode was followed. The results of the tracing process are illustrated in figure 19.

https://doi.org/10.1017/jfm.2015.135 Published online by Cambridge University Press

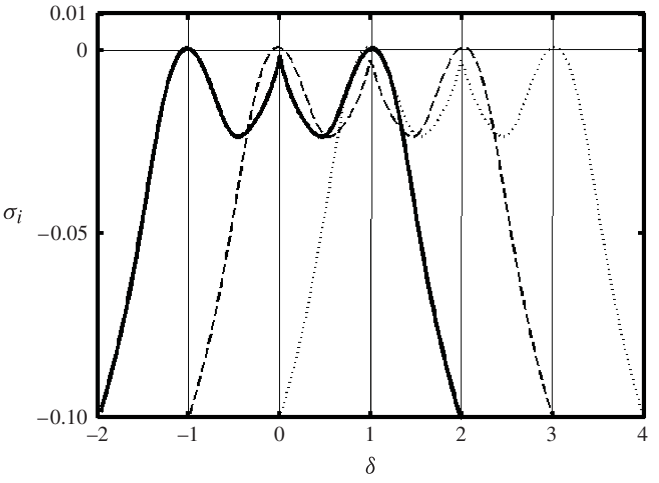


FIGURE 19. Variations of the amplification rate σ_i as a function of δ for $S = 0.005$, $\alpha = 1$, $Re = 6000$ and the fixed flow rate constraint. The maximum amplification for these conditions corresponds to $\delta = 1.04$. Solid, dashed and dotted lines identify three families of solutions corresponding to δ, $\delta + \alpha$, $\delta + 2\alpha$. Vertical lines mark boundaries between Brillouin zones. Results of tracing for the TS wave in a smooth channel overlap with the solid line within the resolution of this figure.

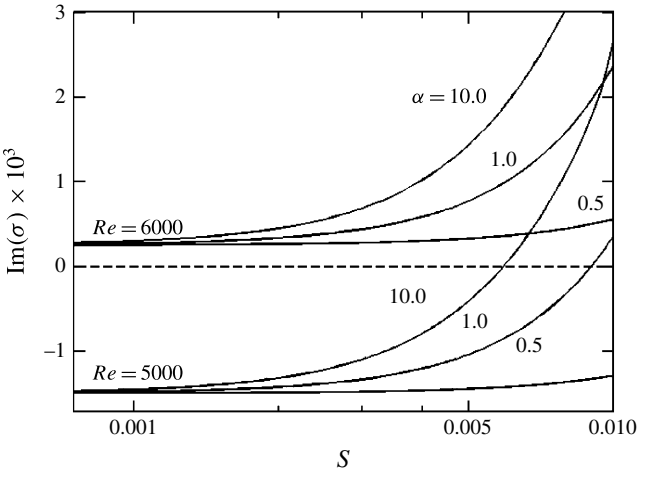


FIGURE 20. Variations of the amplification rate σ_i for the two-dimensional TS wave with $\delta = 1.04$ as a function of S for the fixed flow rate constraint.

The results displayed in figure 20 demonstrate that meandering destabilizes TS waves, with its effectiveness rapidly increasing with S. Figure 21 illustrates variations of the amplification rates as a function of α for a fixed S and a subcritical $Re = 5000$, and demonstrates that an increase of α causes more pronounced destabilization. Use of large α results in an effective narrowing of the channel opening (see § 2.2), with the flow lifting above the ridges and becoming nearly rectilinear (see figure 3). The flow accelerates as the same mass flow has to pass through a narrower channel,

https://doi.org/10.1017/jfm.2015.135 Published online by Cambridge University Press

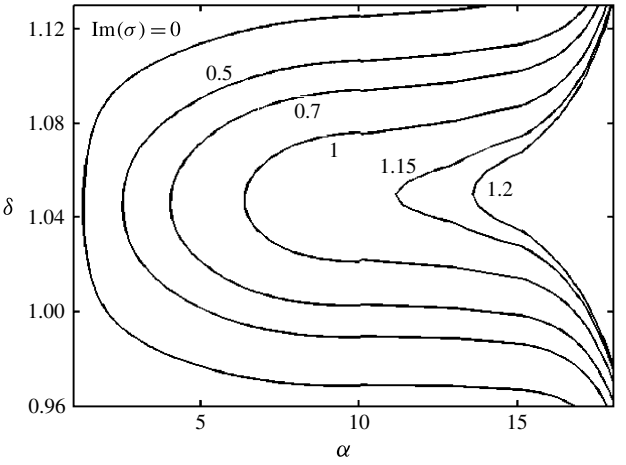


FIGURE 21. Variations of the amplification rate σ_i of the two-dimensional TS waves as a function of α and δ for $S = 0.008$, $Re = 5000$ and the fixed flow rate constraint.

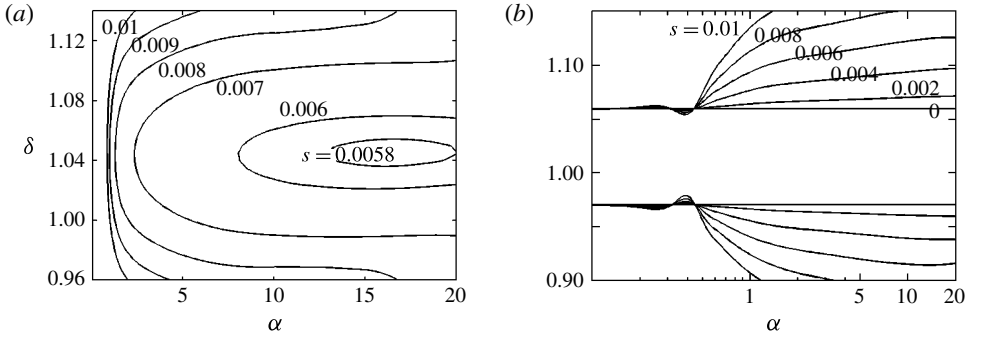


FIGURE 22. The neutral stability curves for the two-dimensional TS waves as a function of δ and α for (*a*) $Re = 5000$ and (*b*) $Re = 6000$ for the fixed flow rate constraint.

but Re remains the same due to the fixed flow rate constraint. The destabilization is associated with the change of the character of the wall layers but details of the mechanics of the flow response remain to be delineated. This particular limit is of no interest in the current analysis as the meandering effect is either reduced or eliminated under such conditions. Figure 22(*a*) displays the neutral stability curves for the same subcritical $Re = 5000$ but for different amplitudes of meandering. Reduction of S shifts the unstable region towards larger α and eventually leads to the complete stabilization of TS waves. Figure 22(*b*) displays the neutral stability curves for the supercritical $Re = 6000$. One can see expansion of the range of unstable δ with an increase of S, with this expansion being more pronounced for larger α. Figure 23 displays variations of the neutral stability curves due to changes of Re. As expected, a sufficient reduction of Re stabilizes the TS waves. Figure 24 displays the neutral curves for the oblique waves and demonstrates that the two-dimensional waves retain their critical role in the meandering channel.

https://doi.org/10.1017/jfm.2015.135 Published online by Cambridge University Press

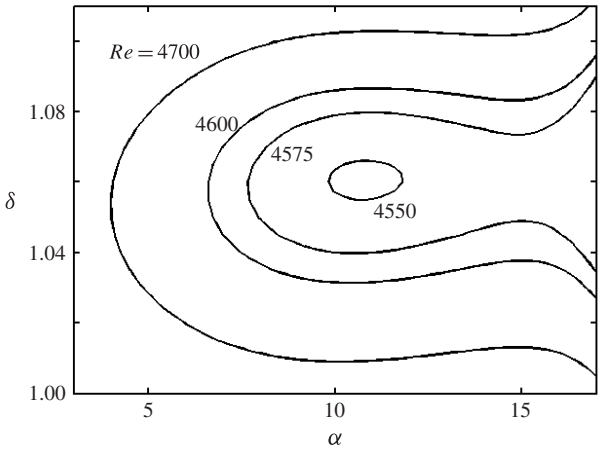


FIGURE 23. The neutral stability curves for the two-dimensional TS waves as a function of δ and α for $S = 0.008$ and the fixed flow rate constraint.

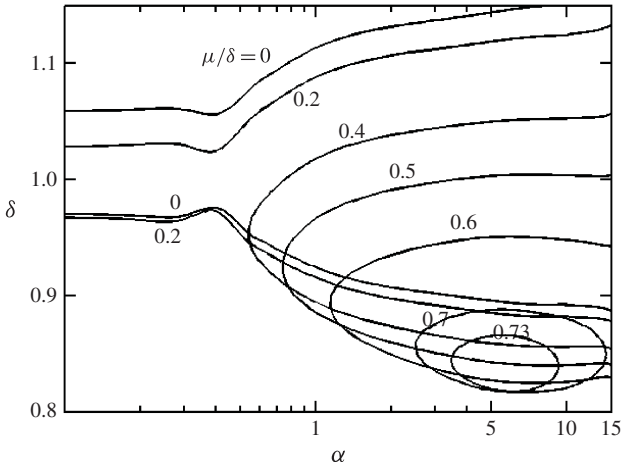


FIGURE 24. The neutral stability curves for the oblique TS waves as a function of δ and α for $S = 0.008$, $Re = 6000$ and the fixed flow rate constraint.

3.4. *Competition between the travelling wave mode and the vortex mode*

The presence of two instability mechanisms raises the question of when each of them will dominate the instability process. Figure 25 presents variations of the global critical $Re_{g,cr}$ as a function of S for both types of instability. The reader may recall that $Re_{g,cr}$ corresponds to the minimum of Re_{cr} over all α for a fixed S. The global critical curves cross each other at $(S, Re_{g,cr}) = (0.00642, 4870)$ for the fixed flow rate constraint and (0.00638, 4935) for the fixed pressure gradient constraint. The crossing points correspond in the case of TS waves to $\alpha = 14.6$ (fixed flow rate) and $\alpha = 13.3$ (fixed pressure gradient) and to $\alpha = 2.95$ for vortices for both types of constraint.

A closer look at the competition between the two modes is provided by the data displayed in figure 26(*a*). It can be seen that Re_{cr} decreases with an increase of S for both modes; this decrease is more rapid for the vortices than for the TS waves but only as long as the meandering wavelength is neither too short nor too long. S needs

https://doi.org/10.1017/jfm.2015.135 Published online by Cambridge University Press

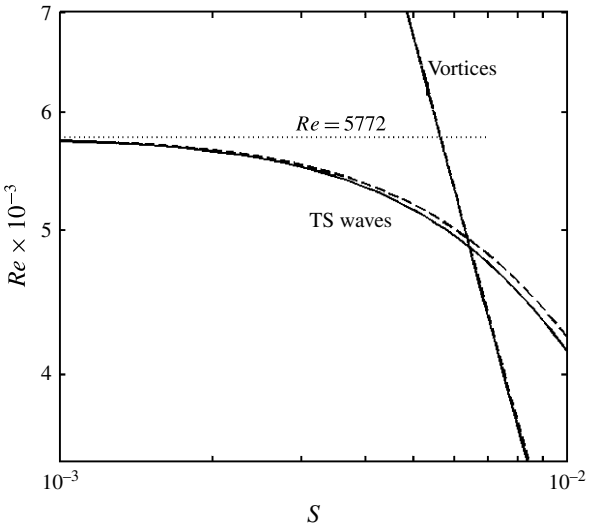


FIGURE 25. Variations of the global critical Reynolds number $Re_{g,cr}$ for the vortex and TS wave modes as functions of S. The solid and dashed lines correspond to the fixed flow rate and the fixed pressure gradient constraints, respectively.

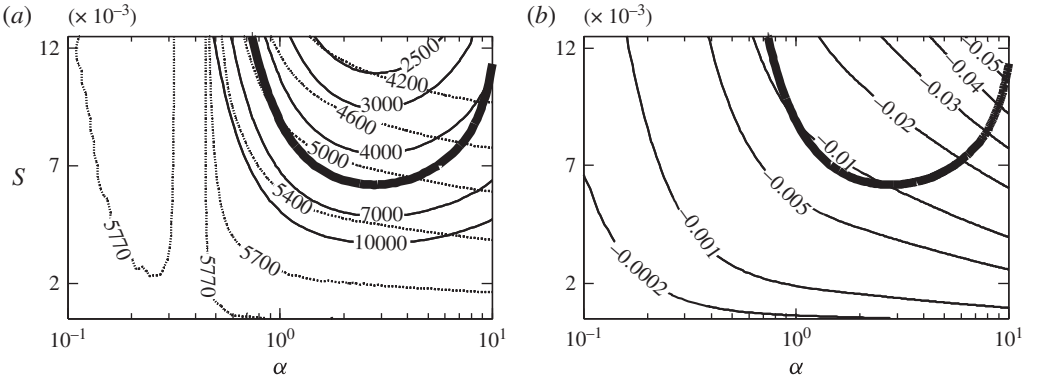


FIGURE 26. (*a*) Variations in the critical Reynolds number Re_{cr} for the onset of the vortex (solid lines) and the TS wave (dashed lines) instabilities, and (*b*) the pressure gradient correction corresponding to the onset of the vortex instability, as functions of S and α. The parameter range indicated by the thick line identifies geometries where the vortex mode plays a critical role.

to reach a minimum of about $S = 0.006$ for Re_{cr} for the two modes to become equal (at $Re_{cr} \approx 5300$) and this occurs for $\alpha \approx 2.5$. Further increase of S builds up the advantage for the vortices. At $S = 0.0125$, Ra_{cr} for the vortices is reduced to $Re_{cr} \approx 2000$ but Ra_{cr} for the TS waves is reduced to only $Re_{cr} \approx 4000$. It is therefore possible to select a meandering geometry that will lead to the formation of the vortices without interference from the TS waves. The large difference between Re_{cr} for the two instability modes for properly selected channel geometry suggests that the accidental setting of TS waves can be avoided. Figure 26(*b*) illustrates pressure losses due to meandering for conditions corresponding to the onset of the vortex mode. In

https://doi.org/10.1017/jfm.2015.135 Published online by Cambridge University Press

general, one should strive to select smaller α, as meandering with long wavelengths generates significantly reduced pressure losses; α cannot be too small as the flow becomes progressively more rectilinear, the centrifugal force field weakens and the vortex mode loses its advantage.

4. Summary

A comprehensive analysis of pressure-driven flow in a meandering channel has been presented. This is the first analysis of this type to the best of the author's knowledge. Sinusoidal meandering around a straight reference axis has been used as a convenient reference case. Its geometry is completely parametrized in terms of the meandering amplitude S and the meandering wavelength $2\pi/\alpha$. The flow conditions are parametrized in terms of the Reynolds number Re based on half of the average channel height. The flow is allowed to develop either with the fixed mass flow rate constraint or the fixed pressure gradient constraint. Flow in a straight channel with the same Re is used as the reference flow.

A detailed analysis of the pressure losses has been carried out. These losses decrease proportionally with α^2 for the long meandering wavelengths and, in the case of short meandering wavelengths, they approach a limiting value associated with the narrowing of the effective channel opening. The magnitude of the losses increases proportionally with S^2 for a sufficiently small meandering amplitude.

It has been shown that the centrifugal effect destabilizes the flow, resulting in the formation of streamwise vortices. The analysis has focused on the smallest meandering amplitude that can lead to the formation of such vortices since, in this case, the vortices can be produced with the smallest pressure loss. Several modes of vortex instability have been identified, with the two dominant modes studied in detail. The first, most unstable mode is driven by two primary vortices attached to walls that are 'outer' with respect to flow turning direction. The primary vortices, which exist only in areas where the flow turning takes place, drive a single secondary vortex in the central section of the channel; this vortex persists throughout the whole channel. The second mode is driven by two similar primary vortices which drive two layers of secondary vortices in the central section of the channel. For each amplitude S, there is a finite band of 'active' meandering wavelengths $2\pi/\alpha$ that gives rise to the instability. Meandering wavelengths that are too long result in a nearly rectilinear flow, and this leads to elimination of the vortices. Meandering wavelengths that are too short also lead to a nearly rectilinear flow via the stream lift-up effect, and therefore also lead to elimination of the vortices. The strength of the instability, as measured by the amplification rate, increases with an increase of S and Re, and the range of α capable of producing instability expands. The critical flow conditions leading to the onset of instability can be found for each combination of S and α. The global critical conditions leading to the onset of instability for any S regardless of α have been determined. The global critical Reynolds number decreases from $Re_{g,cr} \approx 5500$ for $S \approx 10^{-3}$ to $Re_{g,cr} \approx 1000$ for $S \approx 0.02$. The flow that develops with the fixed mass flow rate constraint is slightly more unstable when compared with the flow driven by the fixed pressure gradient. This difference increases with an increase of the meandering amplitude S.

Formation of the vortices can be affected by the appearance of shear-driven instabilities, i.e. TS waves. These waves, once established, can prevent formation of the vortices. A detailed analysis of shear-driven instability has been carried out for the same channel. It has been shown that the two-dimensional waves remain

https://doi.org/10.1017/jfm.2015.135 Published online by Cambridge University Press

critical. The most effective α for the formation of this instability is, by an order of magnitude, larger than the most effective α for the centrifugal instability. Comparison of the two instabilities demonstrates that the meandering geometry that is the most effective in the creation of the vortices does not promote travelling wave instability. It is therefore possible to use channel meandering for the creation of the vortices while avoiding triggering of the travelling waves and thus potentially avoiding initiation of the laminar–turbulent transition process. The presented results probably apply to other geometrical forms of meanderings if one invokes the reduced geometry model concept.

Acknowledgements

This work has been carried out with support of the Natural Sciences and Engineering Research Council (NSERC) of Canada. The author would like to thank Dr E. Savory for proofreading the manuscript and Drs H. V. Moradi, S. Krol and A. Mohammadi for assistance with supplementary computations.

Appendix A. Analysis of flow in the small-amplitude limit ($S \to 0$)

Analysis of the mean flow begins with the regularization of the flow domain using a transformation of the form $\eta = y - 2S\cos(\alpha x)$, which leads to field equations of the form

$$\frac{\partial u_b}{\partial x} + 2S\alpha \sin(\alpha x)\frac{\partial u_b}{\partial \eta} + \frac{\partial v_b}{\partial \eta} = 0, \tag{A 1a}$$

$$\begin{aligned} -\left(1 + 4S^2\alpha^2 \sin^2(\alpha x)\right)\frac{\partial^2 u_b}{\partial \eta^2} - \frac{\partial^2 u_b}{\partial x^2} - 4S\alpha \sin(\alpha x)\frac{\partial^2 u_b}{\partial x \partial \eta} - 2S\alpha^2 \cos(\alpha x)\frac{\partial u_b}{\partial \eta} \\ + 2S\alpha Re\ \sin(\alpha x)\, u_b\frac{\partial u_b}{\partial \eta} + Re\, v_b\frac{\partial u_b}{\partial \eta} + Re\, u_b\frac{\partial u_b}{\partial x} \\ + Re\frac{\partial p_b}{\partial x} + 2S\alpha\, Re \sin(\alpha x)\frac{\partial p_b}{\partial \eta} = 0, \end{aligned} \tag{A 1b}$$

$$\begin{aligned} -\left(1 + 4S^2\alpha^2 \sin^2(\alpha x)\right)\frac{\partial^2 v_b}{\partial \eta^2} - \frac{\partial^2 v_b}{\partial x^2} - 4S\alpha \sin(\alpha x)\frac{\partial^2 v_b}{\partial x \partial \eta} - 2S\alpha^2 \cos(\alpha x)\frac{\partial v_b}{\partial \eta} \\ + 2S\alpha Re\ \sin(\alpha x)\, u_b\frac{\partial v_b}{\partial \eta} + Re\, v_b\frac{\partial v_b}{\partial \eta} + u_b\frac{\partial u_b}{\partial x} + Re\frac{\partial p_b}{\partial \eta} = 0, \end{aligned} \tag{A 1c}$$

$$u_b = v_b = 0 \quad \text{at } \eta = \pm 1, \qquad Q_b = \int_{-1}^{1} u_b(x, \eta)\mathrm{d}\eta = \frac{4}{3}. \tag{A 1d,e}$$

The solution can be represented in the form

$$u_b = \tilde{u}_0 + S\tilde{u}_1 + S^2\tilde{u}_2 + O(S^3), \qquad v_b = S\tilde{v}_1 + S^2\tilde{v}_2 + O(S^3), \tag{A 2a,b}$$

$$p_b = \tilde{p}_0 + S\tilde{p}_1 + S^2\tilde{p}_2 + O(S^3), \qquad Q_b = Q_0, \tag{A 2c,d}$$

where

$$\tilde{u}_0 = (1 - \eta^2), \qquad \tilde{p}_0 = -2Re^{-1}x + \text{const.}, \qquad Q_0 = 4/3. \tag{A 3a–c}$$

Extraction of the two leading-order terms leads to the system $O(S)$ of the form

$$\frac{\partial \tilde{u}_1}{\partial x} + \frac{\partial \tilde{v}_1}{\partial \eta} = -\alpha\ \sin(\alpha x)\frac{\mathrm{d}u_0}{\mathrm{d}\eta}, \tag{A 4a}$$

https://doi.org/10.1017/jfm.2015.135 Published online by Cambridge University Press

$$\frac{\partial^2\tilde{u}_1}{\partial x^2}+\frac{\partial^2\tilde{u}_1}{\partial \eta^2}-Re\frac{\partial\tilde{p}_1}{\partial x}-Re\ u_0\frac{\partial\tilde{u}_1}{\partial\eta}-Re\ \frac{\mathrm{d}u_0}{\mathrm{d}\eta}\tilde{v}_1$$
$$=-\alpha^2\ \cos(\alpha x)\frac{\mathrm{d}u_0}{\mathrm{d}\eta}+\alpha\, Re\sin(\alpha x)u_0\frac{\mathrm{d}u_0}{\mathrm{d}\eta}, \tag{A 4b}$$
$$\frac{\partial^2\tilde{v}_1}{\partial x^2}+\frac{\partial^2\tilde{v}_1}{\partial \eta^2}-Re\frac{\partial\tilde{p}_1}{\partial \eta}-Re\ u_0\frac{\partial\tilde{v}_1}{\partial x}=0, \tag{A 4c}$$
$$\tilde{u}_1(\pm1)=0,\quad \tilde{v}_1(\pm1)=0,\quad \int_{-1}^{1}\tilde{u}_1(\xi,\eta)\mathrm{d}\eta=0 \tag{A 4d–f}$$

and the system $O(S^2)$ of the form

$$\frac{\partial\tilde{u}_2}{\partial x}+\frac{\partial\tilde{v}_2}{\partial\eta}=-\alpha\sin(\alpha x)\frac{\partial\tilde{u}_1}{\partial\eta}, \tag{A 5a}$$
$$\frac{\partial^2\tilde{u}_2}{\partial x^2}+\frac{\partial^2\tilde{u}_2}{\partial \eta^2}-Re\frac{\partial\tilde{p}_2}{\partial x}-Re\ u_0\frac{\partial\tilde{u}_2}{\partial\eta}-Re\ \frac{\mathrm{d}u_0}{\mathrm{d}\eta}\tilde{v}_2$$
$$=\alpha\, Re\sin(\alpha x)\frac{\partial\tilde{p}_1}{\partial\eta}-\alpha^2\ \cos(\alpha x)\frac{\partial\tilde{u}_1}{\partial\eta}-2\alpha\sin(\alpha x)\frac{\partial^2\tilde{u}_1}{\partial x\partial\eta}-\alpha^2\sin^2(\alpha x)\frac{\mathrm{d}^2u_0}{\mathrm{d}\eta^2}$$
$$+Re\,\tilde{u}_1\frac{\partial\tilde{u}_1}{\partial x}+\alpha\, Re\sin(\alpha x)u_0\frac{\partial\tilde{u}_1}{\partial\eta}+\alpha\, Re\sin(\alpha x)\frac{\mathrm{d}u_0}{\mathrm{d}\eta}+\tilde{v}_1\frac{\partial\tilde{v}_1}{\partial\eta}, \tag{A 5b}$$
$$\frac{\partial^2\tilde{v}_2}{\partial x^2}+\frac{\partial^2\tilde{v}_2}{\partial \eta^2}-Re\frac{\partial\tilde{p}_2}{\partial\eta}-Re\ u_0\frac{\partial\tilde{v}_2}{\partial x}$$
$$=-\alpha^2\cos(\alpha x)\frac{\partial\tilde{v}_1}{\partial\eta}-2\alpha\sin(\alpha x)\frac{\partial^2\tilde{v}_1}{\partial x\partial\eta}+Re\,\tilde{u}_1\frac{\partial\tilde{v}_1}{\partial x}+\alpha\, Re\sin(\alpha x)u_0\frac{\partial\tilde{v}_1}{\partial\eta}, \tag{A 5c}$$
$$\tilde{u}_2(\pm1)=0,\quad \tilde{v}_2(\pm1)=0,\quad \int_{-1}^{1}\tilde{u}_2(x,\eta)\mathrm{d}\eta=0. \tag{A 5d–f}$$

The solution of (A 4) has the form

$$\left[\tilde{u}_1(x,\eta),\tilde{v}_1(x,\eta),\tilde{p}_1(x,\eta)\right]=\left[\tilde{u}_1^{(1)}(\eta),\ \tilde{v}_1^{(1)}(\eta),\ \tilde{p}_1^{(1)}(\eta)\right]\mathrm{e}^{\mathrm{i}\alpha x}$$
$$+\left[\tilde{u}_1^{(-1)}(\eta),\ \tilde{v}_1^{(-1)}(\eta),\ \tilde{p}_1^{(-1)}(\eta)\right]\mathrm{e}^{-\mathrm{i}\alpha x}, \tag{A 6}$$

where $\tilde{u}_1^{(-1)},\tilde{v}_1^{(-1)},\tilde{p}_1^{(-1)}$ are complex conjugates of $\tilde{u}_1^{(1)},\tilde{v}_1^{(1)},\tilde{p}_1^{(1)}$. Substitution of (A 6) into (A 4), separation of Fourier modes and elimination of $\tilde{u}_1^{(1)}$ and $\tilde{p}_1^{(1)}$ lead to a problem for $\tilde{v}_1^{(1)}$ of the form

$$\left(D^2-\alpha^2\right)^2\tilde{v}_1^{(1)}-\mathrm{i}\alpha Re\,u_0D^2\tilde{v}_1^{(1)}+\mathrm{i}\alpha\, Re\left(\frac{\mathrm{d}^2u_0}{\mathrm{d}\eta^2}+\alpha^2u_0\right)\tilde{v}_1^{(1)}$$
$$=-\frac{\mathrm{i}\alpha^3}{2}\frac{\mathrm{d}^2u_0}{\mathrm{d}\eta^2}-\frac{\alpha^2Re}{2}\frac{\mathrm{d}u_0}{\mathrm{d}\eta}-\frac{\alpha^2Re}{2}\left[\left(\frac{\mathrm{d}u_0}{\mathrm{d}\eta}\right)^2-u_0\frac{\mathrm{d}^2u_0}{\mathrm{d}\eta^2}\right] \tag{A 7a}$$
$$\tilde{v}_1^{(1)}(1)=0,\quad \tilde{v}_1^{(1)}(-1)=0,\quad D\tilde{v}_1^{(1)}(1)=-\frac{\mathrm{i}\alpha}{2}\frac{\mathrm{d}u_0}{\mathrm{d}\eta}\bigg|_{\eta=1}, \tag{A 7b–d}$$
$$D\tilde{v}_1^{(1)}(-1)=-\frac{\mathrm{i}\alpha}{2}\frac{\mathrm{d}u_0}{\mathrm{d}\eta}\bigg|_{\eta=-1}, \tag{A 7e}$$

https://doi.org/10.1017/jfm.2015.135 Published online by Cambridge University Press

which has been solved numerically using the spectral collocation method. Determination of $\tilde{u}_1^{(1)}$ and $\tilde{p}_1^{(1)}$ is done *a posteriori* using the following formulae:

$$\left.\begin{aligned} \tilde{u}_1^{(1)} &= \frac{\mathrm{i}}{\alpha} D\tilde{v}_1^{(1)} - \frac{1}{2}\frac{\mathrm{d}u_0}{\mathrm{d}\eta}, \\ \tilde{p}_1^{(1)} &= -\frac{\mathrm{i}}{\alpha\, Re} D^2\tilde{u}_1^{(1)} + \left(\frac{\mathrm{i}\alpha}{Re} - u_0\right)\tilde{u}_1^{(1)} + \frac{\mathrm{i}}{\alpha}\frac{\mathrm{d}u_0}{\mathrm{d}\eta}\tilde{v}_1^{(1)} - \frac{\mathrm{i}\alpha}{2\,Re}\frac{\mathrm{d}u_0}{\mathrm{d}\eta} + \frac{1}{2}u_0\frac{\mathrm{d}u_0}{\mathrm{d}\eta}. \end{aligned}\right\} \tag{A 8}$$

The solution of (A 5) has the form

$$\left[\tilde{u}_2(x,\eta), \tilde{v}_2(x,\eta), \tilde{p}_2(x,\eta) - Ax\right] = \sum_{n=-2}^{n=2}\left[\tilde{u}_2^{(n)}(\eta), \tilde{v}_2^{(n)}(\eta), \tilde{p}_2^{(n)}(\eta)\right]\mathrm{e}^{\mathrm{i}n\alpha x}. \tag{A 9}$$

Substitution of (A 9) into (A 5) and extraction of mode zero leads to the system

$$D\tilde{v}_2^{(0)} = g_1, \quad D^2\tilde{u}_2^{(0)} - A\,Re - Re\frac{\mathrm{d}u_0}{\mathrm{d}\eta}\tilde{v}_2^{(0)} = g_2, \quad D^2\tilde{v}_2^{(0)} - Re\,D\tilde{p}_2^{(0)} = g_3, \tag{A 10a–c}$$

$$\int_{-1}^{1}\tilde{u}_2^{(0)}\mathrm{d}\eta = 0, \quad \tilde{u}_2^{(0)}(\pm 1) = \tilde{v}_2^{(0)}(\pm 1) = 0, \tag{A 10d,e}$$

where

$$g_1 = -\frac{\mathrm{i}\alpha}{2} D\left(\tilde{u}_1^{(-1)} - \tilde{u}_1^{(1)}\right), \tag{A 11a}$$

$$g_2 = -\frac{\mathrm{i}\,Re}{2} D\left(\tilde{p}_0^{(-1)} - \tilde{p}_0^{(1)}\right) + \frac{\mathrm{i}\alpha}{2} D^2\left(\tilde{v}_1^{(1)} - \tilde{v}_1^{(-1)}\right) - \alpha^2\frac{\mathrm{d}^2u_0}{\mathrm{d}\eta^2} - \frac{1}{2}Re\,D\left[u_0 D\left(\tilde{v}_1^{(1)} + \tilde{v}_1^{(-1)}\right)\right] + Re\,D\left(\tilde{v}_1^{(1)}\tilde{v}_1^{(-1)}\right), \tag{A 11b}$$

$$g_3 = \frac{\alpha^2}{2} D\left(\tilde{v}_1^{(-1)} + \tilde{v}_1^{(1)}\right) + Re\,D\left(\tilde{v}_1^{(-1)} + \tilde{v}_1^{(1)}\right) + \frac{\mathrm{i}\alpha\,Re}{2}\frac{\mathrm{d}u_0}{\mathrm{d}\eta}\left(\tilde{v}_1^{(-1)} - \tilde{v}_1^{(1)}\right) - \frac{\mathrm{i}\alpha\,Re}{2} u_0 D\left(\tilde{v}_1^{(-1)} - \tilde{v}_1^{(1)}\right). \tag{A 11c}$$

The above system can be solved, resulting in

$$\tilde{v}_2^{(0)} = -\tfrac{1}{2} D\left(\tilde{v}_1^{(1)} + \tilde{v}_1^{(-1)}\right), \tag{A 12a}$$

$$\tilde{u}_2^{(0)} = \frac{1}{2}Re\,A\left(\eta^2 - 1\right) + \int_{-1}^{\eta} K(\theta)\mathrm{d}\theta - \frac{1}{2}(\eta + 1)\int_{-1}^{1} K(\eta)\mathrm{d}\eta, \tag{A 12b}$$

$$Re\,\tilde{p}_2^{(0)} = -\left(\frac{1}{2}D^2 + \frac{\alpha^2}{2} + Re\right)\left(\tilde{v}_1^{(1)} + \tilde{v}_1^{(-1)}\right) + \frac{\mathrm{i}\alpha Re}{2} u_0\left(\tilde{v}_1^{(-1)} - \tilde{v}_1^{(1)}\right) - \mathrm{i}\alpha\,Re\int\frac{\mathrm{d}u_0}{\mathrm{d}\eta}\left(\tilde{v}_1^{(-1)} - \tilde{v}_1^{(1)}\right)\mathrm{d}\eta + \mathrm{const.} \tag{A 12c}$$

$$Re\,A = \frac{3}{2}\int_{-1}^{1}\left[\int_{-1}^{\eta} K(\theta)\mathrm{d}\theta\right]\mathrm{d}\eta, \tag{A 12d}$$

where

$$K(\eta) = -\frac{Re}{2}\int_{-1}^{\eta}\frac{\mathrm{d}u_0}{\mathrm{d}\eta} D(\tilde{v}_1^{(1)} + \tilde{v}_1^{(-1)})\mathrm{d}\eta - \frac{\mathrm{i}\alpha\,Re}{2}\left(\tilde{p}_1^{(-1)} - \tilde{p}_1^{(1)}\right) + \frac{\mathrm{i}\alpha}{2} D\left(\tilde{v}_1^{(1)} - \tilde{v}_1^{(-1)}\right) - \alpha^2\frac{\mathrm{d}u_0}{\mathrm{d}\eta} - \frac{1}{2}Re\,u_0 D\left(\tilde{v}_1^{(1)} + \tilde{v}_1^{(-1)}\right) + Re\,\tilde{v}_1^{(1)}\tilde{v}_1^{(-1)}. \tag{A 12e}$$

https://doi.org/10.1017/jfm.2015.135 Published online by Cambridge University Press

Solution (A 12) demonstrates that the change in the pressure gradient is generated by the nonlinear effects, and it increases proportionally with S^2 for sufficiently small S. A similar solution can be worked out for the fixed pressure gradient case (not shown).

Appendix B. Convergence of numerical solution

Number of Fourier modes for disturbances	Number of Fourier modes for mean	Number of Fourier modes for mean flow (79 Chebyshev polynomials used)		
		3	5	7
3	3	0.168768791	0.169193745	0.169215278
5	3	0.167289249	0.167574616	0.167590673
5	5		0.167637413	0.167651963
7	3	0.167332955	0.167632786	0.167647521
7	5		0.167642942	0.167654746
7	7			0.167655776

Number of Chebyshev polynomials (seven Fourier modes used for mean flow and disturbances)				
39	49	59	69	79
0.167813252	0.167652166	0.167655798	0.167655781	0.167655776

TABLE 1. Amplification rate $10^2\sigma_i$ for the first vortex mode with $S = 0.02$, $\alpha = 3$, $Re = 1500$, $\mu = 2$ and flow subject to the fixed flow rate constraint.

Number of Fourier modes for disturbances	Number of Fourier modes for mean	Number of Fourier modes for mean flow (79 Chebyshev polynomials used)		
		3	5	7
3	3	0.778953847	0.778954112	0.778954112
5	3	0.778953437	0.778953703	0.778953703
5	5		0.778953693	0.778953693
7	3	0.778953437	0.778953703	0.778953703
7	5		0.778953693	0.778953693
7	7			0.778953693

Number of Chebyshev polynomials (seven Fourier modes used for mean flow and disturbances)				
39	49	59	69	79
0.779289007	0.778955138	0.778953655	0.778953655	0.778953693

TABLE 2. Amplification rate $10^3\sigma_i$ for the TS wave with $\delta = 1.024$, $S = 0.005$, $\alpha = 1$, $Re = 6000$ and flow subject to the fixed flow rate constraint.

Appendix C. Solution of the vortex stability problem in the limit $S \to 0$

It can be shown that equations (3.7) take the following form in the limit $S \to 0$:

$$A^{(m)}\zeta_y^{(m)} + Bg_v^{(m)} = 0, \quad C^{(m)}g_v^{(m)} = 0. \tag{C 1a,b}$$

https://doi.org/10.1017/jfm.2015.135 Published online by Cambridge University Press

Each pair of the above equations describes disturbances of periodicity $2\pi/m\alpha$ and $2\pi/\mu$ in the streamwise and spanwise directions, respectively. Equation (C 1*a*) describes the so-called Squire modes, and (C 1*b*) describes the so-called Tollmien–Schlichting (TS) modes. Streamwise vortices correspond to $m = 0$ as they are independent of x. In this case, equations (C 1*a*) and (C 1*b*) reduce to the form independent of α, i.e.

$$(D^2 - \mu^2 + \mathrm{i}\,Re\,\sigma)g_u^{(0)} - Re\,Du_0\,g_v^{(0)} = 0, \quad (D^2 - \mu^2)(D^2 - \mu^2 + \mathrm{i}\,Re\,\sigma)\,g_v^{(0)} = 0. \tag{C 2a,b}$$

The homogeneous part of (C 3), supplemented by the homogeneous boundary conditions at $y = \pm 1$, represents an eigenvalue problem describing Squire modes which has symmetric and asymmetric families of solutions. All of the symmetric solutions are attenuated and have the form

$$g_u^{(0)} = c_1\,\cos[(\pi/2 + n\pi)y], \quad g_v^{(0)} = g_w^{(0)} = 0, \quad \sigma = -\mathrm{i}\,\left[\mu^2 + (\pi/2 + n\pi)^2\right]/Re, \tag{C 3a–c}$$

where c_1 is an arbitrary constant. The least attenuated solution corresponds to $n = 0$. All asymmetric solutions are also attenuated and have the form

$$g_u^{(0)} = c_2\,\sin(n\pi y), \quad \sigma = -\mathrm{i}\,(\mu^2 + n^2\pi^2)/Re, \tag{C 4a,b}$$

where c_2 is an arbitrary constant. The least attenuated solution corresponds to $n = 1$. Equation (C 4), supplemented by the homogeneous boundary conditions, represents an eigenvalue problem describing the TS modes. The symmetric solutions, which are all attenuated, have the form

$$g_v^{(0)} = c_1\left[\cos(\theta y) - \frac{\cos(\theta)}{\cosh(\mu)}\cosh(\mu y)\right], \quad \sigma = -\mathrm{i}\,(\theta^2 + \mu^2)/Re, \tag{C 5a,b}$$

where θ is a root of $[\theta\,\sin(\theta)\,\cosh(\mu) + \mu\,\sinh(\mu)\,\cos(\theta)] = 0$ and c_1 is an arbitrary constant. The smallest positive roots that lead to the least stable solution have numerical values equal to 2.4809, 2.3271 for $\mu = 2$, 2.5, respectively. The asymmetric solutions have the form

$$g_v^{(0)} = c_2\left[\sin(\theta y) - \frac{\sin(\theta)}{\sinh(\mu)}\sinh(\mu y)\right], \quad \sigma = -\mathrm{i}\,(\theta^2 + \mu^2)/Re, \tag{C 6a,b}$$

where θ is a root of $[\theta\,\cos(\theta)\,\sinh(\mu) - \mu\,\cosh(\mu)\,\sin(\theta)] = 0$ and c_2 is an arbitrary constant. The smallest positive roots that lead to the least stable solutions have numerical values equal to 4.2591, 4.1659 for $\mu = 2$, 2.5, respectively.

REFERENCES

BAI, Y. C. & YANG, Y. H. 2011 The dynamic stability of the flow in a meander channel. *Sci. China, Technol. Sci.* **54**, 931–940.

BERGLES, A. E., JENSEN, M. K. & SHOME, B. 1996 The literature on enhancement of convective heat and mass transfer. *J. Enhanced Heat Transfer* **4**, 1–6.

BERGLES, A. E. & WEBB, R. L. 1985 A guide to the literature on convective heat transfer augmentation. In *Advances in Heat Transfer 1985* (ed. S. M. Shenkman, J. E. O'Brien, I. S. Habib & J. A. Kohler), ASME Symposium, HTD, vol. 43, pp. 81–90.

https://doi.org/10.1017/jfm.2015.135 Published online by Cambridge University Press

BLOCH, F. 1928 Über die Quantenmechanik der Elektronen in Kristallgittern. *Z. Phys.* **52**, 555–600.

CASTELAIN, C., MOKRANI, A., LEGENTILHOMME, P. & PEERHOSSAINI, H. 1997 Residence time distribution in twisted pipe flows: helically coiled system and chaotic system. *Exp. Fluids* **22**, 359–368.

CASTELAIN, C., MOKRANI, A., LE GUER, Y. & PEERHOSSAINI, H. 2001 Experimental study of chaotic advection regime in a twisted duct flow. *Eur. J. Mech.* B **20**, 205–232.

CODDINGTON, E. A. & LEVINSON, N. 1965 *Theory of Ordinary Differential Equations*. McGraw-Hill.

COLOMBINI, M. & PARKER, G. 1995 Longitudinal streaks. *J. Fluid Mech.* **304**, 161–183.

DEAN, W. 1928 Fluid motion in a curved channel. *Proc. R. Soc. Lond.* A **121**, 402–412.

FIEBEG, M. 1995*a* Vortex generators for compact heat exchangers. *J. Enhanced Heat Transfer* **2**, 43–61.

FIEBEG, M. 1995*b* Embedded vortices in internal flow: heat transfer and pressure loss enhancement. *Intl J. Heat Fluid Flow* **16**, 376–388.

FIEBEG, M. 1998 Vortices, generators and heat transfer. *Chem. Engng Res. Des.* **76**, 108–123.

FIEBEG, M. & CHEN, Y. 1999 Heat transfer enhancement by wing-type longitudinal vortex generators and their application to finned oval tube heat exchanger elements. In *Heat Transfer Enhancement of Heat Exchangers* (ed. S. Kakaç, A. E Bergles, F. Mayinger & H. Yüncü), pp. 79–105. Kluwer.

FLORYAN, J. M. 1986 Görtler instability of boundary layers over concave and convex walls. *Phys. Fluids* **29**, 2380–2387.

FLORYAN, J. M. 1991 On the Görtler instability of boundary layers. *Prog. Aeronaut. Sci.* **28**, 235–271.

FLORYAN, J. M. 1997 Stability of wall-bounded shear layers in the presence of simulated distributed surface roughness. *J. Fluid Mech.* **335**, 29–55.

FLORYAN, J. M. 2002 Centrifugal instability of Couette flow over a wavy wall. *Phys. Fluids* **14**, 312–322.

FLORYAN, J. M. 2003 Vortex instability in a converging–diverging channel. *J. Fluid Mech.* **482**, 17–50.

FLORYAN, J. M. 2007 Three-dimensional instabilities of laminar flow in a rough channel and the concept of hydraulically smooth wall. *Eur. J. Mech.* B **26**, 305–329.

FLORYAN, J. M. & ASAI, M. 2011 On the transition between distributed and isolated surface roughness and its effect on the stability of channel flow. *Phys. Fluids* **23**, 104101.

GONG, L., KOTA, K., TAO, W. & JOSHI, Y. 2011 Parametric numerical study of flow and heat transfer in microchannels with wavy walls. *Trans. ASME J. Heat Transfer* **133**, 051702.

GÖRTLER, H. 1941 Instabilität laminarer Grenzschichten an konkaven Wänden gegenüber gewissen dreidimensionalen Störungen. *Z. Angew. Math. Mech.* **21**, 250–252.

GSCHWIND, P., REGELE, A. & KOTTKE, V. 1995 Sinusoidal wavy channels with Taylor–Görtler vortices. *Exp. Therm. Sci.* **11**, 270–275.

GUZMÁN, A. M., CÁRDENAS, M. J., URZÚA, F. A. & ARAYA, P. E. 2009 Heat transfer enhancement by flow bifurcation in asymmetric wavy wall channels. *Intl J. Heat Mass Transfer* **52**, 3778–3789.

HERBERT, T. 1988 Secondary instability of boundary layers. *Annu. Rev. Fluid Mech.* **20**, 487–526.

HOSSAIN, M. Z., FLORYAN, D. & FLORYAN, J. M. 2012 Drag reduction due to spatial thermal modulations. *J. Fluid Mech.* **713**, 398–419.

HUSAIN, S. Z. & FLORYAN, J. M. 2010 Spectrally-accurate algorithm for moving boundary problems for the Navier–Stokes equations. *J. Comput. Phys.* **229**, 2287–2313.

HUSAIN, S. Z. & FLORYAN, J. M. 2013 Effective solvers for the immersed boundaries method. *Comput. Fluids* **84**, 127–140.

HUSAIN, S. Z., FLORYAN, J. M. & SZUMBARSKI, J. 2009 Over-determined formulation of the immersed boundary conditions method. *J. Comput. Meth. Appl. Mech. Engng* **199**, 94–112.

IKEDA, S., PARKER, G. & SAWAI, K. 1981 Bend theory of river meanders. Part 1. Linear development. *J. Fluid Mech.* **112**, 363–377.

JACOBI, A. M. & SHAH, R. K. 1995 Heat transfer surface enhancement through the use of longitudinal vortices: a review of recent progress. *Exp. Therm. Fluid Sci.* **11**, 295–309.

https://doi.org/10.1017/jfm.2015.135 Published online by Cambridge University Press

LIGRANI, P. M., OLIVEIRA, M. M. & BLASKOVITCH, T. 2003 Comparison of heat transfer augmentation techniques. *AIAA J.* **41**, 337–362.

LOH, S. A. & BLACKBURN, H. M. 2011 Stability of steady flow through an axially corrugated pipe. *Phys. Fluids* **23**, 111703.

MACK, L. M. 1976 A numerical study of the temporal eigenvalue spectrum of the Blasius boundary layer. *J. Fluid Mech.* **73**, 497–520.

METWALLY, H. M. & MANGLIK, R. M. 2004 Enhanced heat transfer due to curvature-induced lateral vortices in laminar flows in sinusoidal corrugated-plate channels. *Intl J. Heat Mass Transfer* **47**, 2283–2292.

MOHAMMADI, A. & FLORYAN, J. M. 2012 Mechanism of drag generation by surface corrugation. *Phys. Fluids* **24**, 013602.

MOHAMMADI, A. & FLORYAN, J. M. 2013*a* Pressure losses in grooved channels. *J. Fluid Mech.* **725**, 23–54.

MOHAMMADI, A. & FLORYAN, J. M. 2013*b* Groove optimization for drag reduction. *Phys. Fluids* **25**, 113601.

MORADI, H. & FLORYAN, J. M. 2013*a* Flows in annuli with longitudinal grooves. *J. Fluid Mech.* **716**, 280–315.

MORADI, H. & FLORYAN, J. M. 2013*b* Maximization of heat transfer across micro-channels. *Intl J. Heat Mass Transfer* **66**, 517–530.

NISHIMURA, T., MURAKAMI, S., ARAKAWA, S. & KAWAMURA, Y. 1990*a* Flow observations and mass transfer characteristics in symmetrically wavy-walled channels at moderate Reynolds numbers for steady flow. *Intl J. Heat Mass Transfer* **33**, 835–845.

NISHIMURA, T., YANO, K., YOSHINO, T. & KAWAMURA, Y. 1990*b* Occurrence and structure of Taylor–Görtler vortices induced in two-dimensional wavy channels for steady flow. *J. Chem. Engng Japan* **23**, 697–703.

OVIEDO-TOLENTINO, F., ROMERO-MÉNDEZ, R., HERNÁNDEZ-GUERRERO, A. & GIRÓN-PALOMARES, B. 2008 Experimental study of fluid flow in the entrance of a sinusoidal channel. *Intl J. Heat Fluid Flow* **29**, 1233–1239.

PARKER, G. 1976 On the cause and characteristic scales of meandering and braiding in rivers. *J. Fluid Mech.* **76**, 457–480.

PARKER, G. & ANDREWS, E. D. 1986 On the time development of meander bends. *J. Fluid Mech.* **162**, 139–156.

PARKER, G., SAWAI, K. & IKEDA, S. 1982 Bend theory of river meanders. Part 2. Nonlinear deformation of finite-amplitude bends. *J. Fluid Mech.* **115**, 303–314.

PATERA, A. T. & MIKIC, B. B. 1986 Exploiting hydrodynamic instabilities: Resonant heat transfer enhancement. *Intl J. Heat Mass Transfer* **29**, 1127–1138.

PHAM, M. V., PLOURDE, F. & DOAN, S. K. 2008 Turbulent heat and mass transfer in sinusoidal wavy channels. *Intl J. Heat Fluid Flow* **29**, 1240–1257.

RAYLEIGH, L. 1920 On the dynamics of revolving fluids. *Sci. Pap.* **6**, 447–453.

ROSAGUTI, N. R., FLETCHER, D. F. & HAYNES, B. S. 2007 Low-Reynolds number heat transfer enhancement in sinusoidal channels. *Chem. Engng Sci.* **62**, 694–702.

RUSH, T. A., NEWELL, T. A. & JACOBI, A. M. 1999 An experimental study of flow and heat transfer in sinusoidal wavy passages. *Intl J. Heat Mass Transfer* **42**, 1541–1553.

SAAD, Y. 2003 *Iterative Methods for Sparse Linear Systems*. SIAM.

SARIC, W. S. & BENMALIK, A. 1991 Görtler vortices with periodic curvature. In *FED,* vol. 114, Boundary Layer and Transition to Turbulence, pp. 37–45. ASME.

SCHMID, P. J. 2007 Nonmodal stability theory. *Annu. Rev. Fluid Mech.* **39**, 129–162.

SUI, Y., TEO, C. J. & LEE, P. S. 2012 Direct numerical simulation of fluid flow and heat transfer in periodic wavy channels with rectangular cross-sections. *Intl J. Heat Mass Transfer* **55**, 73–88.

SZUMBARSKI, J. & FLORYAN, J. M. 1999 A direct spectral method for determination of flows over corrugated boundaries. *J. Comput. Phys.* **153**, 378–402.

SZUMBARSKI, J. & FLORYAN, J. M. 2006 Transient disturbance growth in a corrugated channel. *J. Fluid Mech.* **568**, 243–272.

https://doi.org/10.1017/jfm.2015.135 Published online by Cambridge University Press

TAYLOR, G. 1923 Stability of viscous liquid contained between two rotating cylinders. *Phil. Trans. R. Soc.* A **223**, 289–293.

WEBB, R. L. & BERGLES, A. E. 1983 Performance evaluation criteria for selection of heat transfer surface geometries used in low Reynolds number heat exchangers. In *Low Reynolds Number Flow Heat Exchangers, Advanced Study Institute Book* (ed. S. Kakaç, R. K. Shah & A. E. Bergles). Hemisphere.

ZHANG, J., KUNDU, J. & MANGLIK, R. M. 2004 Effects of fin waviness and spacing on the lateral vortex structure and laminar heat transfer in wavy-plate-fin core. *Intl J. Heat Mass Transfer* **47**, 1719–1730.

https://doi.org/10.1017/jfm.2015.135 Published online by Cambridge University Press